GEOPHYSICS, VOL. 78, NO. 1 (JANUARY-FEBRUARY 2013); P. D21–D40, 17 FIGS., 7 TABLES.
10.1190/GEO2012-0176.1

Downloaded 01/22/13 to 138.67.207.132. Redistribution subject to SEG license or copyright; see Terms of Use at http://library.seg.org/

Petrophysical properties of saprolites from the Oak Ridge Integrated Field Research Challenge site, Tennessee

André Revil[1], Magnus Skold[2], Susan S. Hubbard[3], Yuxin Wu[3], David B. Watson[4], and Marios Karaoulis[2]

ABSTRACT

At the Oak Ridge Integrated Field Research Challenge site, near Oak Ridge, Tennessee, the shallow saprolitic aquifer is contaminated by nitric acid, uranium, and metals originating from the former S3 settling ponds. To interpret low-frequency geophysical methods used to image contaminant plumes, we have characterized the petrophysical properties of three representative saprolite core samples. Their hydraulic conductivity ranges from 10^{-7} to 10^{-6} m s^{-1} in agreement with field data. Complex conductivity measurements, in the frequency range of 1 mHz to 45 kHz, were performed with NaCl solutions with electrical conductivities in the range 5×10^{-3} to 2.35 S m^{-1}, a range representative of field conditions. The electrical conductivity data were well reproduced with a simple linear conductivity model between the saprolite conductivity and the pore water conductivity. The conductivity plots were used to estimate the formation factor (the cementation exponent was about 2.2 ± 0.3) and the surface conductivity (0.007–0.040 S m^{-1}). The magnitude of the surface conductivity depended on the degree of weathering and therefore on the amount of smectite and mixed layer (illite-smectite) clays present in the saprolite. The chargeability of the core samples was in the range of 20 to 800 mV V^{-1} and is strongly dependent on the salinity. We also performed streaming potential measurements with the same pore fluid composition as that used for the complex conductivity measurements. We found an excess of movable electrical charges on the order of 100 to 500 C m^{-3} in agreement with previous investigations connecting the movable excess charge density to permeability. The zeta potential was in the range of −10 to −20 mV independent on the salinity. The electrical measurements were consistent with an average cation exchange capacity in the range of 1.4 to 11 cmol kg^{-1} and a specific surface area on the order of 4000 to about 30,000 m^2 kg^{-1}.

INTRODUCTION

Various geophysical methods have been used to locate contaminant migration at the Oak Ridge Integrated Field Research Challenge (IFRC) site, near Oak Ridge, Tennessee (USA) (Watson et al., 2005; Chen et al., 2006, 2010; Kowalsky et al., 2011; Gasperikova et al., 2012). The IFRC was established as a part of the U. S. Department of Energy (DOE) Subsurface Biogeochemistry Research program to evaluate different remediation technologies. The S3 settling basins are located in the Bear Creek Valley at the western edge of the Y-12 plant belonging to the Oak Ridge Reservation of the U. S. DOE. These basins consisted of four ponds built in 1951. For the following 32 years, they received a yearly volume of 7.6 million liters of acidic (pH < 2) liquid wastes consisting of nitric acid, uranium, technetium, cadmium, mercury, chlorinated solvents, and strontium among other harmful species (Gu et al., 2003). The contaminants from the S3 basins have infiltrated the shallow saprolitic aquifer resulting in plumes extending up to 5 km downgradient from the basins' location. Many of the geophysical studies performed at the IFRC relied on site-specific empirical relationships. To improve the quantitative interpretation of low-frequency geoelectrical data (direct-current [DC] resistivity,

Manuscript received by the Editor 11 May 2012; revised manuscript received 23 September 2012; published online 14 December 2012.
[1]Université de Savoie, ISTerre, Le Bourget du Lac, France; Colorado School of Mines, Department of Geophysics, Golden, Colorado, USA. E-mail: arevil@mines.edu.
[2]Colorado School of Mines, Department of Geophysics, Golden, Colorado, USA. E-mail: mskold@mines.edu; marios.karaoulis@gmail.com.
[3]Lawrence Berkeley National Laboratory, Berkeley, California, USA. E-mail: sshubbard@lbl.gov; ywu3@lbl.gov.
[4]Oak Ridge National Laboratory, Oak Ridge, Tennessee, USA. E-mail: watsondb@ornl.gov.
© 2012 Society of Exploration Geophysicists. All rights reserved.

Downloaded 01/22/13 to 138.67.207.132. Redistribution subject to SEG license or copyright; see Terms of Use at http://library.seg.org/

induced polarization, and self-potential), there is a need to understand at a more fundamental level the petrophysical properties of the saprolite.

The present work concerns the development of a database of various petrophysical measurements of saprolitic core samples from the uncontaminated IFRC background location. These samples were collected from the same geologic formation as the former S3 ponds and share the same characteristics of the saprolite as the contaminated area. In this paper, we present a comparison between recently derived petrophysical models and this new set of petrophysical measurements including permeability, complex conductivity, and streaming potential data on saprolite cores samples.

MATERIAL AND METHODS

Saprolitic materials

The contaminated and uncontaminated areas are situated near the Y-12 National Security Complex in Bear Creek Valley in Oak Ridge, Tennessee (Figure 1). The shallow subsurface consists of saprolites, which result from the weathering of Middle Cambrian interbedded shale, siltstone, and limestone forming the parent rock material (Figure 1c; Driese et al., 2001; Watson et al., 2004). It overlies the calcite-rich Nolichucky shale formation, which is part of the Cambrian Conasauga Group, located in the Bear Creek Valley.

A number of publications describe the mineralogy of the saprolite and some of their properties at the IFRC (e.g., Jardine et al., 1993a, 1993b). Despite the fact that there are some variations in the clay content with depth, the sand and silt fractions (in weight) are grossly 50% and 31%, respectively, and the clay fraction is about 19% (Jardine et al., 1988, 1993a, 1993b). The cation exchange capacity of saprolite soil samples collected at 1 m depth is typically 10.5 cmol kg^{-1} (0.105 meq g^{-1}; see Kim et al., 2009). Jardine et al. (1993a) report a CEC in the range 7 to 16 cmol kg^{-1} (0.07–0.16 meq g^{-1}). Waxman and Smits (1968) develop the following relationship between the CEC and the specific area $S_{Sp} = NeCEC/(Q_S)$, where $Q_S = 0.32$ C m^{-2} (Revil et al., 1998; Woodruff and Revil, 2011) denotes the charge per unit surface area for clays and the CEC expressed in C kg^{-1}. Taking 10.5 cmol kg^{-1} is therefore consistent with a specific surface area of about 30,000 m^2 kg^{-1}. This value is itself fairly consistent with the reactive surface area of the saprolite from Oak Ridge as Kooner et al. (1995) measure, 40,000 m^2 kg^{-1}, and as shown below, it agrees with our own estimates.

According to Kim et al. (2009), quartz, illite, and microcline (K-feldspar) make up 95% of the total mineral composition. The main component of the minor fraction (remaining 5%) is vermiculite, a 2:1 clay mineral. Taking 5% weight fraction of vermiculite with a CEC of 1 meq g^{-1} (1 mol kg^{-1}) implies that the weight fraction of illite, with a CEC of 0.20 meq g^{-1} (20 cmol kg^{-1}), is 28% on average (see CEC values in Lipsicas, 1984; Zundel and Siffert, 1985). The percentage of vermiculite increases with weathering and therefore with depth. The grain density is assumed to be equal to 2650 kg m^{-3} and the porosity decreases with depth from ~0.50 close to the ground surface to ~0.25 at a depth of 5 m (Driese, 2002).

Several saprolite core samples from the background (upgradient) location, near the Oak Ridge National Laboratory (Figure 1b), were collected by augering and a split spoon sampler. The background site is located within the same geologic formation as the former S3 ponds and the collected samples are representative of the contaminated saprolite (same mineralogy and petrophysical properties). Continuous sediment samples were collected in 5 ft long plastic sleeves from just below the ground surface to a depth of approximately 8.2 m. At the background site, the depth of the water table oscillates between 2 to 4 m and the pH of the aquifer is between 4.8 and 6.0. The samples were stored in capped plastic sleeves until use in the laboratory experiments. Groundwater was sampled from monitoring well FW-300 located in the background location. The shallow uncontaminated groundwater at the background site is typically a Ca-HCO_3/MgCa-HCO_3 type groundwater due to the dissolution of calcite and dolomite (Saunders and Toran, 1994). The composition of the groundwater at the background site is given in Table 1 and its electrical conductivity in the range 0.0047–0.0081 S m^{-1} at 25°C.

Three saprolite core samples were collected from 2.7, 4.9, and 6.7 m below the ground surface (Samples S9, S16, and S22, respectively, the number denotes the depth of the sample in ft). The core samples were cut from the original

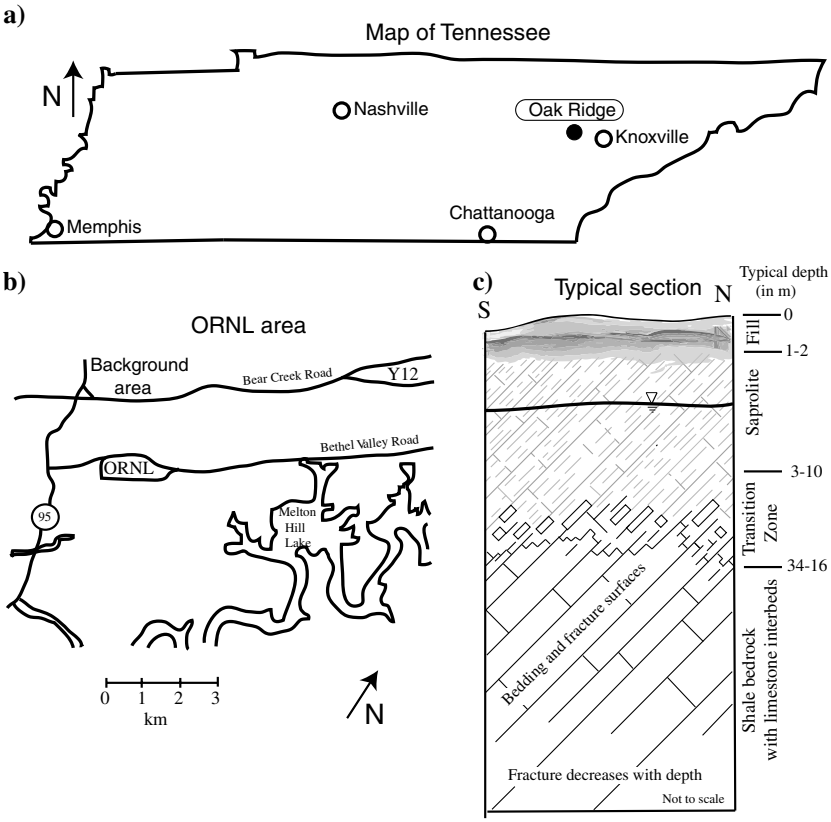

Figure 1. Position of the site from where the samples have been extracted. (a) Position of Oak Ridge in Tennessee. (b) Position of the background site (ORNL: Oak Ridge National Laboratory). (c) Typical section of saprolite and parent rock at the Oak Ridge IFRC site.

Downloaded 01/22/13 to 138.67.207.132. Redistribution subject to SEG license or copyright; see Terms of Use at http://library.seg.org/

plastic sleeves and homogenized in a ball mill for 5 min at 20°C. We check that this process did not crush the grains. Then they were packed into 5 cm long portion of 4.4 cm diameter acrylic columns. These samples were chosen to represent the saprolitic material at different depths above the parent rocks. The end caps of the columns were slotted to distribute the flow evenly across the samples. At mid-height of the samples, four Ag(s)/AgCl electrodes were installed circumferentially at 60° angle for complex conductivity measurements (Figure 2) and two additional Ag(s)/AgCl close to the end faces of the core samples were used to measure the streaming potential. The experimental setup served as a constant head permeameter and was used for all petrophysical measurements. The samples were saturated from the bottom up with background groundwater under vacuum for three days. The porosity of the packed samples was approximately 47% (measured after the experiments by drying the core samples).

The samples were initially flushed with 42–124 pore volumes of background groundwater to establish equilibrium conditions (the volume injected through the samples was accurately measured, and the pore volume estimated from the porosity and the volume of the core samples). Once the electrical conductivity of the influent and effluent solutions was within 20×10^{-4} S m^{-1} of each other and the pH differed less than approximately 0.5 pH units, the hydraulic conductivity, streaming potential coupling coefficient, and complex conductivity were measured. The samples were subsequently flushed with 3, 10, 30, 100, and 300 mM NaCl solutions and a pH close to pH 5.7 and with 10 mM NaCl solutions with pH adjusted to various pH values between 3 and 6 as discussed further below. We found that ~100 pore volumes were flushed through each core sample before equilibrium was reached (the differences of conductivity and pH between the influent and effluent solutions were vanishingly small). The experiments reported in this paper therefore took several months to be completed.

Mineralogical analyses were performed on three background saprolite samples from the same cores and at nearly the same depths as the samples used for petrophysical measurements. The samples were collected from 3.0, 5.1, and 6.9 m below the ground surface (Samples S10, S17, and S23, respectively; the number denotes the depth of the sample in ft). The mineralogical composition of these whole rock samples was analyzed using X-ray diffraction (XRD; Figure 2). The remainder of the samples was disaggregated in deionized water, and the clay-sized fraction was separated by centrifugation. The fraction <0.3 μm was air dried, reacted with ethylene glycol for 1 h, and subsequently heated to 375°C to evaporate the ethylene glycol and collapse the expanded spaces between the smectite clay layers. After each treatment, XRD analyses were performed on samples with the clay layers oriented parallel to the surface of the mounting plate.

Quartz, potassium feldspar, plagioclase, and clay minerals were identified by XRD analyses of the whole rock samples. The XRD analyses did not allow for quantitative analysis of the mineral content. However, the intensity of the reflections of the clay minerals increased with depth while the intensity of the quartz reflection decreased. The intensity of the clay reflections normalized to the intensity of the quartz reflection was approximately 50% greater in Sample S17 compared to Sample S10. The quartz-normalized intensity of the clay reflections of the deepest sample was approximately one order of magnitude greater compared to Sample S10. The clay fractions of all three samples were dominated by illite and mixed clays consisting of 80%–90% illite and 10%–20% smectite (Figure 2). A trace amount of chlorite may be present in Sample S23, but kaolinite or vermiculite were not identified in any sample.

We also performed specific surface area measurements using the Brunauer, Emmett, and Teller (BET) approach (Brunauer et al., 1938) at the Colorado School of Mines. For Samples S7, S15, and S21 (at 7-, 15-, and 21-ft depths), we obtained the following (measured) specific surface areas: $21,670 \pm 30$, $14,980 \pm 20$, and $23,110 \pm 30$ m^2 kg^{-1}.

Petrophysical measurements

Darcy's law is a constitutive equation connecting the volumetric flux of water through a porous material **u** (the Darcy velocity) to the gradient of the pore fluid pressure or hydraulic head. In saturated conditions, Darcy's law is written as (Darcy, 1856)

$$\mathbf{u} = -\frac{k}{\eta_f}\nabla p = -K\nabla h, \tag{1}$$

where k denotes the permeability (in m^2), K is the hydraulic conductivity (in m s^{-1}), p is the pore fluid pressure (in Pa), h is the hydraulic head (in m), and η_f is the dynamic viscosity of the pore water ($\eta_f = 10^{-3}$ Pa s at 25°C). From previous studies (e.g., Salomon et al., 1992; McKay et al., 2005), the permeability of the saprolite is expected to be low but higher than 1 mD (10^{-15} m^2). We can therefore use the constant head permeameter shown in Figure 3 to determine the permeability for a broad range of NaCl solutions (from 3 to 300 mM). The fluxes were measured for different heads, and Darcy's law was used to estimate the permeability.

We performed frequency-domain measurements of the impedance Z^* (in Ω) of the core samples in the frequency range 1 mHz–45 kHz (see Vinegar and Waxman [1984], Slater and Lesmes [2002], and Slater and Glaser [2003] for an in-depth description of some laboratory procedures). The impedance Z^* (in Ω) is given by $Z^*(\omega) = |Z^*(\omega)|e^{i\varphi(\omega)} = U/I$, where U is the

Table 1. Background groundwater composition and properties (from Schreiber, 1995).

Element or property	Value
Ca (mg/L) GW	26–73
Mg (mg/L) GW	1.7–9.4
K (mg/L)	<2.0–3.8
Na (mg/L)	2.7–120
HCO_3 (mg/L)	98–330
Cl (mg/L)	0.9–5.5
SO_4 (mg/L)	6.6–170
Alk. (mg/kg as $CaCO_3$)	80–270
pH	6.9–8.1
Eh (mV)	550[5]
TDS (mg/L)	152–714
Conductivity σ_w (S/m)	0.0047–0.0081[6]

[5]From Jardine et al. (1993b).
[6]This work.

voltage between potential electrodes M and N (Figure 3), I is the magnitude of the current injected between the current electrodes A and B (Figure 3), and $|Z^*(\omega)|$ and $\varphi(\omega)$ denote the amplitude and the phase of the impedance, respectively. The complex resistivity ρ^* is related to Z^* by a geometrical factor G (in m) by $\rho^*(\omega) = GZ^*(\omega)$. The geometrical factor takes into account the position of the electrodes on the sample, its size and shape, and the boundary conditions for the potential. The complex resistivity ρ^* can be recast into the complex conductivity ($\sigma^* = 1/\rho^*$) described in the previous section. The measurements were done with the sample holder shown in Figure 3 during the permeability measurements thus maintaining the same packing.

The measurements were performed with the high-precision impedance meter described by Zimmerman et al. (2008). The accuracy of the instrument is ~0.1–0.3 mrad at frequencies below 1 kHz (see Zimmerman et al. [2008] and Revil and Skold [2011] for various benchmark tests). The geometric factor was determined numerically using COMSOL Multiphysics 4.1 solving the Laplace equation for the electrical potential and using the geometry of the sample holder shown in Figure 3 (see Jougnot et al. [2010] for details). This estimate was consistent with an estimate of the geometric factor obtained by having a solution of known conductivity in the sample holder and performing a measurement of the resistance for the same electrode configuration.

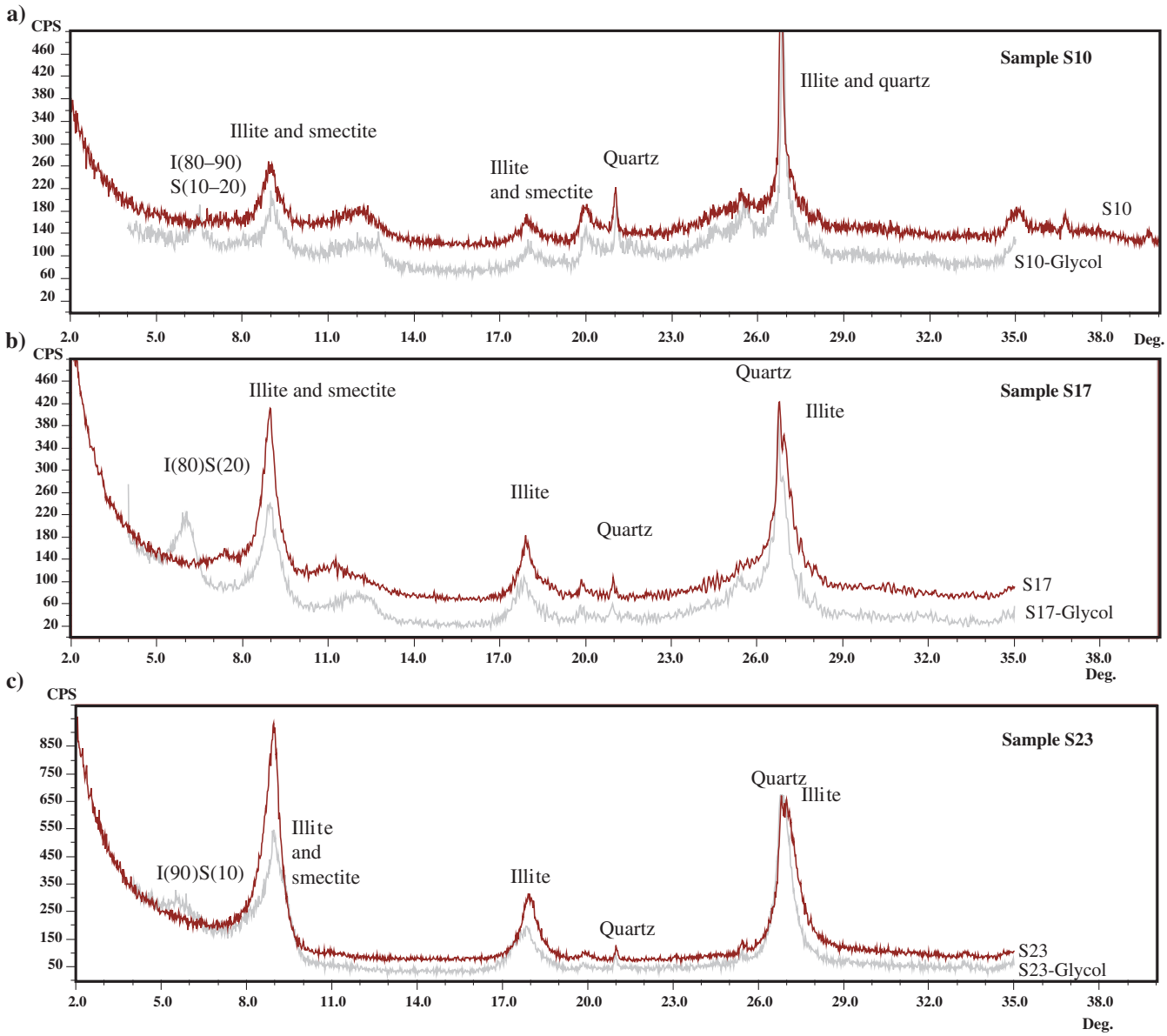

Figure 2. X-ray diffraction analysis. (a) Sample S10. (b) Sample S17. (c) Sample S23. Illite can be identified in all three samples. A mixed layer of illite$_{80}$smectite$_{20}$ is identified for Sample S17. For Sample S23, the peak shift indicates the presence of mixed layer clays (illite$_{90}$smectite$_{10}$). For Sample S23, note the lower intensity of the quartz reflection and the greater intensity of the clay reflections compared to the other two samples. This sample contains significantly more clay than the other two.

Downloaded 01/22/13 to 138.67.207.132. Redistribution subject to SEG license or copyright; see Terms of Use at http://library.seg.org/

Downloaded 01/22/13 to 138.67.207.132. Redistribution subject to SEG license or copyright; see Terms of Use at http://library.seg.org/

The setup for the measurement of the streaming potential coupling coefficient is the same as that used to measure the permeability (Figure 3). To measure the streaming potential coupling coefficient, we use the following protocol. A given hydraulic head is imposed on the cylindrical sample inside the tube by adding water to the water column in the tube in such a way that the hydraulic head is maintained constant. The gradient of the fluid pressure is controlled by the hydraulic head in the tube and the length of the porous pack (typically between 1 to 60 cm). In both cases, the brine is flowing through the porous sample. The resulting electrical potential is measured with two nonpolarizable $Ag/AgCl_2$ electrodes (Ref321/XR300, Radiometer Analytical) located in the vicinity of the end faces of the sample. The difference of the electrical potential measured between the end faces of the porous pack divided by the length of the sample is the streaming electrical field associated with the flow of the solution through the porous sample. The voltages are measured with a data logger (Easy Log, internal impedance of 10 MΩ, sensitivity of 0.1 mV) or with a voltmeter (Metrix MX-20, internal impedance of 100 MΩ, sensitivity of 0.1 mV). Both provided consistent measurements.

PERMEABILITY

The permeability data are shown in Figure 5. The hydraulic conductivities of our core samples range from 10^{-6} to 10^{-7} m s^{-1}, and the corresponding permeabilities are in the range 10^{-13} to 10^{-14} m^2 (100 to 10 mD). For the least concentrated NaCl solution used in our investigations (3 mM NaCl, 1200 μm cm^{-1}, 25°C), the permeability of the core sample ranges from 7 to 16 mD (Table 2). The measured hydraulic conductivities for the different salinities are reported in Tables 3–5 and Figure 5. These permeabilities are comparable to the in situ measurements of the hydraulic conductivity of the saprolite reported by McKay et al. (2005), which range from 10^{-6} to 10^{-9} m s^{-1}. We also

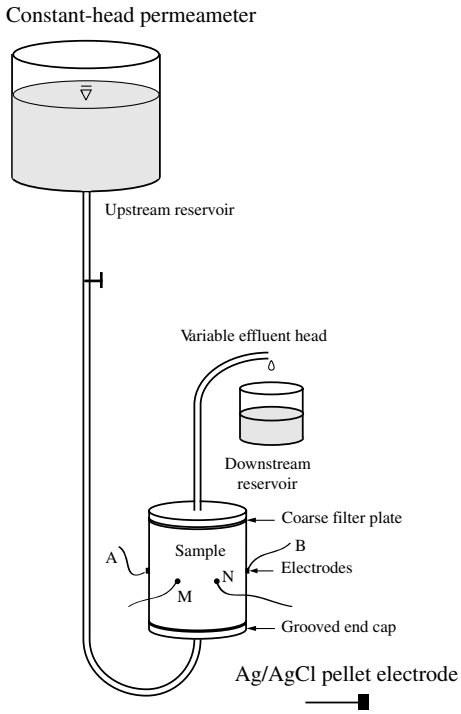

Figure 3. Sketch of the equipment used for the permeability and electrical measurements. Constant head permeameter. The nonpolarizing Ag/AgCl electrodes for the measurement of the complex conductivity are organized in a Wenner array (A and B are the current electrodes, and M and N are the potential electrodes). The electrodes ABMN are located in the middle of the sample holder. The geometrical factor for this array is modeled with COMSOL Multiphysics 3.5a. The nonpolarizing electrodes for the streaming potential measurements are placed at the two end faces of the core sample (not shown here).

Table 2. Petrophysical properties of the three samples (S9, S16, and S22) investigated in this study.

Property	S9	S16	S22
Connected porosity ϕ (-)	0.48	0.49	0.43
Formation factor F (-)	4.1 ± 0.3	5.9 ± 0.1	4.4 ± 0.5
Surface conductivity σ_S (S m^{-1})[7]	$(39 \pm 6) \times 10^{-4}$	$(95 \pm 2) \times 10^{-4}$	$(376 \pm 34) \times 10^{-4}$
Cementation exponent m (-)	1.9	2.5	1.8
Permeability k (m^2)[8]	$(16 \pm 3) \times 10^{-15}$	$(5.0 \pm 3) \times 10^{-15}$	$(7.7 \pm 0.7) \times 10^{-15}$
Excess of charge Q_V (C m^{-3})[9]	3.9×10^6	1.4×10^7	4.2×10^7
CEC (cmol kg^{-1})[10]	1.4	5.3	12
Specific surface area S_{Sp} (m^2 kg^{-1})[11]	4200	15.900	37,000
Specific surface area S_{Sp} (m^2 kg^{-1})[12]	21,670 $\pm$30	14,980 $\pm$20	23,110 $\pm$30
Charge density $\hat{Q}_V$ (C m^{-3})[13]	140	400	490

The reported porosities are the total connected porosity.
[7]At pH values in the range of 5–6.
[8]10 mM NaCl (1200 μm cm^{-1}, 25°C). Average of seven measurements for each sample.
[9]Obtained from the streaming potential data using equation 32.
[10]Using surface conductivity data with $Q_V = F\sigma_S/[\beta_{(+)}(1-f)]$ with $f = 0.924$.
[11]Using $\mathrm{CEC} = 100Q_V\phi/[Ne\rho_g(1-\phi)]$ with $N = 6.02 \times 10^{23}$ Mol^{-1}, $e = 1.6 \times 10^{-19}$ C, and with $Q_V = F\sigma_S/[\beta_{(+)}(1-f)]$ with $f = 0.924$, and the measured porosities.
[12]Using $S_{Sp} = Ne\mathrm{CEC}/(100/Q_S)$ with $Q_S = 0.32$ C m^{-2}.
[13]BET measurements, Samples S7, S15, and S21.

Downloaded 01/22/13 to 138.67.207.132. Redistribution subject to SEG license or copyright; see Terms of Use at http://library.seg.org/

performed experiments at different pH values in the range 3–6 (Figure 5). The hydraulic conductivity of the three core samples does not seem to be dependent on the pH value, but there is a noticeable jump in the hydraulic conductivity above pH 5.6. We have no explanation for this jump.

ELECTRICAL CONDUCTIVITY

When the displacement and conduction current densities are taken together, the combined total current density is (Vinegar and Waxman, 1984)

$$\mathbf{J}_t = (\sigma^* + i\omega\varepsilon_\infty)\mathbf{E}, \tag{2}$$

where $\mathbf{E}$ is the electrical field (in $\mathrm{V\,m^{-1}}$), σ^* is the complex conductivity associated with charge electromigration and accumulation, ω is the angular frequency, and ε_∞ is the high-frequency dielectric constant of the porous material (in $\mathrm{F\,m^{-1}}$). In the following, we will neglect the high-frequency dielectric term and focus on the frequency range of 1 mHz–10 kHz. The complex conductivity is related to the measured conductivity amplitude $|\sigma|$ and the measured phase lag φ by (Seigel, 1959)

$$\sigma^* = |\sigma| \cdot \exp(i\varphi) = \sigma' + i\sigma'', \tag{3}$$

where the amplitude is given by $|\sigma| = \sqrt{\sigma'^2 + \sigma''^2}$ and the phase angle is given by $\varphi = a\ \tan(\sigma''/\sigma') \approx \sigma''/\sigma'(<0)$ (the approximation holds for a phase angle smaller than 100 mrad), i denotes the pure imaginary number, σ' and σ'' denote the in-phase (real) and quadrature (imaginary) components of the complex conductivity, respectively. The in-phase conductivity represents the ability of the porous material to transmit electrical current, whereas the quadrature conductivity describes the ability of the porous material to store reversibly electrical charges.

The physics of induced polarization is, however, not completely clear because several mechanisms of charge storage compete at low frequencies (Schwarz, 1962; Olhoeft, 1985; Revil and Florsch, 2010; Revil, 2012). In the absence of metallic particles such as pyrite or magnetite, the main mechanisms of polarization are possibly related to the polarization of the inner part of the electrical double layer called the Stern layer (Stern, 1924; Leroy et al., 2008; Revil and Florsch, 2010; Vaudelet et al., 2011a, 2011b). Other polarization mechanisms, such as membrane polarization, could contribute to the measured response. The electrical double layer comprises (1) the Stern layer including mobile weakly sorbed counterions that are able to move tangentially along the mineral surface (outer-sphere complex in the terminology used in electrochemistry; the inner-sphere complexes are not mobile because they are strongly sorbed onto the mineral surface) and (2) the diffuse layer of counterions and coions located further in the pore water but still in the vicinity of the mineral/water interface (Figure 4). When an electrical field is applied to a single grain, the cations within the electrical double layer move in the direction of the electric field and accumulate at the edge of the grain; when the electrical field is removed, the chemical gradient causes the cations to diffuse back to equilibrium (e.g., Revil and Florsch, 2010).

Low-frequency induced polarization is usually described in terms of a Cole-Cole distribution given by (e.g., Cole and Cole, 1941; Seigel, 1959; Pelton et al., 1978)

$$\sigma^* = \sigma_\infty\left[1 - \frac{M}{1 + (i\omega\tau_{CC})^\alpha}\right], \tag{4}$$

$$M = \frac{\sigma_\infty - \sigma_0}{\sigma_\infty}, \tag{5}$$

where M ($0 \le M \le 1$) denotes the chargeability (and is usually expressed in mV/V), σ_0 denotes the DC electrical conductivity ($\omega = 0$), σ_∞ is the high-frequency electrical conductivity ($\omega \gg 1/\tau_{CC}$), τ_{CC} denotes the Cole-Cole time constant (in s), α denotes the unitless Cole-Cole exponent, which describes the broadness of the relaxation times distribution. The normalized chargeability is defined as $M_n = M\sigma_\infty = \sigma_\infty - \sigma_0$. The angular frequency of the phase peak (expressed in rad) is given by (Seigel, 1959)

$$\omega_{\mathrm{peak}} = \left(\frac{\sigma_\infty}{\sigma_0}\right)^{1/2\alpha}\frac{1}{\tau_{CC}} = \left(\frac{1}{1-M}\right)^{1/2\alpha}\frac{1}{\tau_{CC}}. \tag{6}$$

If the chargeability M is very small ($\ll$1), then $\omega_{\mathrm{peak}} \approx 1/\tau_{CC}$ and

$$f_{\mathrm{peak}} \approx 1/(2\pi\tau_{CC}). \tag{7}$$

Table 3. Streaming potential coupling coefficient *C* and hydraulic conductivity *K* for Sample S9.

Test	Influent	Influent	C	Effluent	Effluent	K
	σ_w ($\mathrm{S\,m^{-1}}$)	pH	($\mathrm{mV\,m^{-1}}$)	σ_w ($\mathrm{S\,m^{-1}}$)	pH	($\mathrm{m\,s^{-1}}$)
FW-300 (GW)	0.00640	6.60 ± 0.40	−1.65 ± 0.11	0.00495	4.67	1.2000e-07
FW-300 (GW)	0.00723	6.96	−2.02 ± 0.78	0.00495	5.59	7.5000e-07
3 mM NaCl	0.0391	5.40	−1.21 ± 0.29	0.0382	5.41	4.5000e-07
10 mM NaCl	0.1218	5.55	−0.50 ± 0.06	0.121	5.76	5.4000e-07
30 mM NaCl	0.3230	5.69	−0.21 ± 0.05	0.323	4.79	3.8000e-07
100 mM NaCl	0.9030	5.75	−0.09 ± 0.02	0.873	4.69	2.7000e-07
300 mM NaCl	2.544	6.33	−0.05 ± 0.02	2.33	4.61	—

GW stands for the natural groundwater.

Downloaded 01/22/13 to 138.67.207.132. Redistribution subject to SEG license or copyright; see Terms of Use at http://library.seg.org/

The recent model of Revil et al. (2012) yields an explicit function for the DC (σ_0) and high-frequency (σ_∞) conductivities and for the chargeability

$$\sigma_0 = \frac{1}{F}\sigma_w + \sigma_S^0, \tag{8}$$

$$\sigma_\infty = \frac{1}{F}\sigma_w + \sigma_S^\infty. \tag{9}$$

Combining equations 5, 7, and 9, we obtain the following expression of the chargeability

$$M = \frac{F(\sigma_S^\infty - \sigma_S^0)}{\sigma_w + F\sigma_S^\infty}. \tag{10}$$

In these equations, σ_w denotes the pore water conductivity and σ_S^0 and σ_S^∞ denote the low- and high-frequency conductivities of the porous media. Equations 8 and 9 predict a linear relationship between the conductivity of the material and the conductivity of the pore water like in the Waxman and Smits (1968) model. The formation factor F is related to the connected porosity ϕ by

$$F = \phi^{-m}, \tag{11}$$

with m denoting the cementation exponent (Archie, 1942).

The complex conductivity spectra of Samples S8, S16, and S22 are displayed in Figure 6. The in-phase conductivity generally increases with the frequency and with the electrical conductivity of the pore water. The in-phase and quadrature conductivity data used for the analysis are reported in Table 6. We use the following relationship to fit the data at a given frequency

$$\sigma' = \frac{1}{F}\sigma_w + \sigma_S. \tag{12}$$

Equation 12 is able to fit the (in-phase) conductivity data at 1 Hz very well ($R = 0.97$) to 0.99 for the three samples (see Figure 7a and 7b), and it is used to determine the formation factor F and the surface conductivity σ_S at 1 H by fitting the conductivity data with a linear least-squares method. The fitted values of the (intrinsic) formation factor and surface conductivity (see fit in Figure 7a, 7b) are reported in Table 2.

The value of the formation factor ranges from 4 to 6 in agreement with the value determined from field data from Watson et al. (2005) (see Figure 7d). In Table 2, the cementation exponent is therefore estimated from the porosity and the formation factor using $m = -\ln F/\ln\phi$. Using the formation factors and porosities given in Table 2, we obtain $m = 2.2 \pm 0.3$.

The surface conductivity σ_S is found to be in the range of 0.004 to 0.038 S m^{-1}. The highest surface conductivity value is associated with Sample S22, which has the highest clay content and probably a relatively high CEC value. This is consistent with the fact that the CEC of smectite is very high (around 1 meq g^{-1}, ~1 mol kg^{-1}). This high CEC is therefore responsible for a very high surface conductivity (see Vinegar and Waxman, 1984; Revil et al., 1998; Revil, 2012). To understand at a more fundamental level these values of surface conductivity, we need a model connecting the surface conductivity to the CEC. Surface conductivity can be given by the following first-order approximation of the model developed by Revil (2012) for high-porosity materials

$$\sigma_S = \frac{1}{F}\beta_{(+)}(1-f)Q_V, \tag{13}$$

$$Q_V = \rho_g\left(\frac{1-\phi}{\phi}\right)\mathrm{CEC}, \tag{14}$$

where f is the fraction of counterions in the Stern layer (also called the "partition coefficient" by Revil and Florsch, 2010) and ρ_g is the grain density. Equation 13 means that the surface conductivity is controlled by the diffuse layer with a fraction of counterions (1-f) (see Figure 3) and a mobility of the counterions $\beta_{(+)}$ equal to the mobility of the counterions in the bulk pore water. On average for illite and smectite, we have $f = 0.90$ (see Revil, 2012). Equation 14 is from Waxman and Smits (1968) and is used to determine the total (Stern plus diffuse layers) volumetric charge density per unit pore volume. This equation is used to compute the volumetric charge density using CEC = 10.5 cmol kg^{-1} and ρ_g = 2650 kg m^{-3} as discussed above and $\phi = 0.46$ (see Table 2); we

Table 4. Streaming potential coupling coefficient *C* and hydraulic conductivity *K* for Sample S16.

Test	Influent	Influent	C	Effluent	Effluent	K
	σ_w (S m^{-1})	pH	(mV m^{-1})	σ_w (S m^{-1})	pH	m s^{-1}
FW-300 (GW)	0.00640	6.60 ± 0.40	−1.43 ± 0.05	0.00606	6.65	7.4000e-05
FW-300 (GW)	0.00723	6.96	−1.17 ± 0.67	0.00580	6.57	1.8000e-07
3 mM NaCl	0.0391	5.40	−1.17 ± 0.09	0.0388	5.97	1.3000e-07
10 mM NaCl	0.1218	5.55	−0.63 ± 0.02	0.121	5.82	3.2000e-07
30 mM NaCl	0.3230	5.69	−0.29 ± 0.03	0.322	5.73	8.9000e-08
100 mM NaCl	0.9030	5.75	−0.13 ± 0.01	0.883	5.81	1.3000e-07
300 mM NaCl	2.544	6.33	−0.040 ± 0.02	2.35	5.72	—

GW stands for the natural groundwater.

obtain $Q_V = 3.1 \times 10^7$ C m^{-3}. Using equation 13 with $f \approx 0.90$, $\beta_{(+)}(\mathrm{Na}^+, 25°\mathrm{C}) = 5.2 \times 10^{-8}$ m^2 s^{-1} V^{-1} (the value of the mobility for sodium in the pore water), $F = 5$ (Table 2), we obtain a surface conductivity $\sigma_S = 0.033$ S m^{-1}, in good agreement with the value of surface conductivity for Sample S22 (0.038 S m^{-1}). Smaller values for the two other samples imply smaller values of the CEC on the order of 1 cmol kg^{-1}.

From Figure 7a and 7b, we observe that at low pore water electrical conductivities, the electrical conductivity of the saprolite is higher than that of the pore water. The data, therefore, show a critical pore water conductivity at which the conductivity of the porous material is equal to the conductivity of the pore water. This point is called the "isoconductivity point" in electrochemistry. The three core samples exhibit an isoconductivity point (see Figure 7a, 7b). This means that the conductivity of a porous aprolite can be higher than the conductivity of its pore water. This type of observation has strong implications in the interpretation of resistivity tomograms in fresh-water environments, a point often missed by hydrogeophycists.

The Dukhin number is defined as the ratio of surface to pore water electrical conductivity (Dukhin and Shilov, 2002). It can be used to normalize the conductivity data by plotting the electrical conductivity of the porous material normalized by the electrical conductivity of the pore water versus the Dukhin number. In this

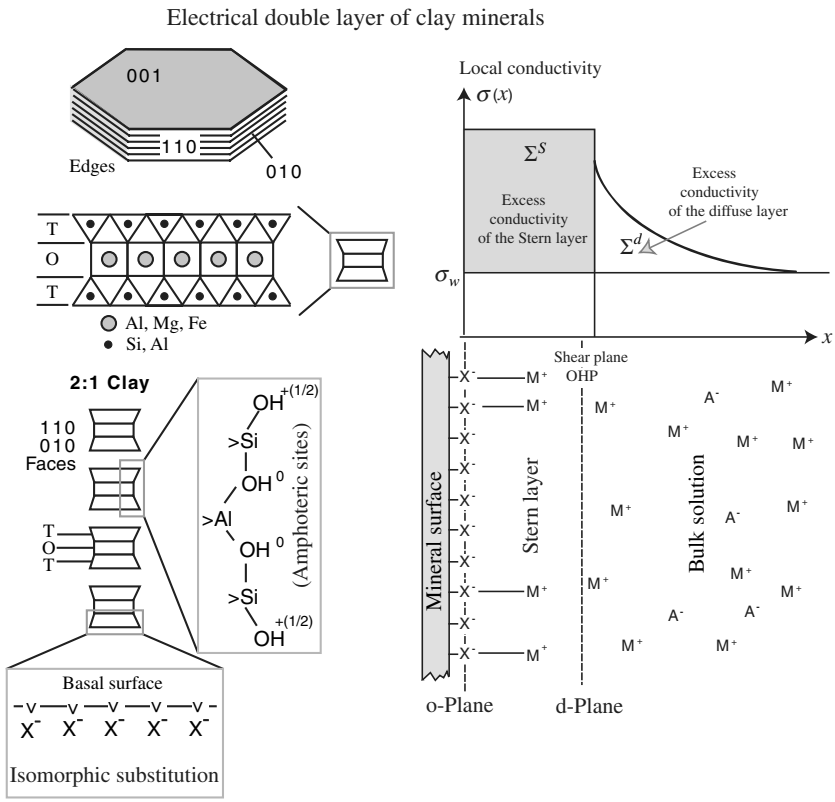

Figure 4. Electrical double layer at the surface of clay minerals. The surface charge of illite and smectite is heterogeneous with amphoteric sites located on the 110 and 010 crystalline planes and isomorphic substitutions in the crystalline framework associated with negative charges on the basal surfaces 001. The electrical double layer is formed of the Stern layer of sorbed counterions and the diffuse layer. The o-plane defines the mineral surface, whereas the d-plane defined the interface between the Stern layer and the diffuse layer on the 110 and 010 crystalline planes. The specific surface conductivities Σ_S and Σ_d define the excess surface conductivity associated with the Stern and diffuse layers with respect to the conductivity of the pore water. The counterions are partitioned between the Stern layer and the diffuse layer, and f denotes the partition coefficient (modified from Revil, 2012).

Table 5. Streaming potential coupling coefficient and permeability for Sample S22.

Test	Influent	Influent	C	Effluent	Effluent	K
	σ_w (S m^{-1})	pH	(mV m^{-1})	σ_w (S m^{-1})	pH	m s^{-1}
FW-300 (GW)	0.00640	6.60 ± 0.40	—	0.00953	7.15	1.6000e-08
FW-300 (GW)	0.00723	6.96	—	0.00709	7.03	2.7000e-07
3 mM NaCl	0.0391	5.40	−0.22 ± 0.11	0.0401	6.36	6.2000e-07
10 mM NaCl	0.1218	5.55	−0.18 ± 0.08	0.122	6.80	1.0300e-06
30 mM NaCl	0.3230	5.69	−0.13 ± 0.04	0.327	5.96	3.8000e-07
100 mM NaCl	0.9030	5.75	−0.10 ± 0.02	0.879	6.23	4.6000e-07
300 mM NaCl	2.544	6.33	−0.05 ± 0.02	2.34	6.03	—

GW stands for the natural groundwater.

Downloaded 01/22/13 to 138.67.207.132. Redistribution subject to SEG license or copyright; see Terms of Use at http://library.seg.org/

Downloaded 01/22/13 to 138.67.207.132. Redistribution subject to SEG license or copyright; see Terms of Use at http://library.seg.org/

case, all the data for various samples with the same formation factor collapse on the same trend. This trend is well reproduced by equation 12 (see Figure 7c). The electrical conductivity of the background groundwater at 25°C is 0.0047–0.0081 $\mathrm{S\,m^{-1}}$, which means that for all the samples, we are below the isoconductivity point for the groundwater conductivity and therefore the in situ conductivity of the saprolite is higher than the conductivity of the pore water. This shows the limit of neglecting surface conductivity to interpret the resistivity tomogram in the field.

The quadrature conductivity data are shown in Figure 6 as a function of the frequency for different pore water conductivities, and the values at 1 H are given in Table 6. The absolute value of the quadrature conductivity increases with the pore water conductivity (Figure 8a, 8b) as predicted by the model of Revil (2012). The quadrature conductivity increases by one order of magnitude when the pore water conductivity increases from 5×10^{-3} to 2.35 $\mathrm{S\,m^{-1}}$ (NaCl).

Sample S16 is the only sample exhibiting a clear relaxation peak for the quadrature conductivity (Sample S9 seems to show two small peaks). The peak frequency is around 10 H and seems independent of the salinity as reported before in the literature for sands (Revil and Skold, 2011; Weller et al., 2011). The magnitude of the quadrature conductivities increase with the salinity (Figure 8a, 8b). For these samples, the Cole-Cole parameters were inverted using a simulated annealing approach (Figure 8c, 8d). We used the strategy called "threshold acceptance" (Dueck and Scheuer, 1990) and its implementation in Mathematica (function NMinimize). The Cole-Cole parameters were used to determine the chargeabilities for each salinity and pH. The inverted chargeability values are shown as a function of the pore water conductivity in Figure 8e. Equation 9 provides a very good fit to the data. In Figure 8f, we show that the Cole-Cole relaxation time is independent on the pore water conductivity, which is consistent with equation 10.

Following Revil (2012), the quadrature conductivity can be expressed as

$$\sigma'' = -\frac{1}{F}\beta^S_{(+)} f Q_V. \tag{15}$$

This means that the polarization is controlled by the Stern layer with a fraction of counterions f (see Figure 3) and a mobility for these counterions $\beta^S_{(+)}$. At high porosities, the formation factor can be approximated by the following equation (Revil and Florsch, 2010):

$$F = 1 + \frac{3}{2}\left(\frac{1-\phi}{\phi}\right) \approx \frac{3}{2}\left(\frac{1-\phi}{\phi}\right). \tag{16}$$

The approximation used in equation 16 corresponds to $F \gg 1$, and therefore $F\text{-}1 \approx F$. Combining equations 14 to 16 yields the following expression between the quadrature conductivity and the CEC (see Revil, 2012):

$$\sigma'' \approx -\frac{2}{3}\beta^S_{(+)} f \rho_g \mathrm{CEC}. \tag{17}$$

Taking $\beta^S_{(+)}(25°\mathrm{C}, \mathrm{Na}^+) = 1.5\times10^{-10}\ \mathrm{m^2\,s^{-1}\,V^{-1}}$, $f = 0.90$, and $\rho_g = 2650\ \mathrm{kg\,m^{-3}}$, we obtain $\sigma'' \approx -a\mathrm{CEC}$ with $a \approx (2/3)\beta^S_{(+)} f \rho_g = 2.4\times10^{-7}\ \mathrm{S\,kg\,C^{-1}\,m^{-1}}$. Starting with equation 17 and using the relationship between the CEC and the specific surface area given above, Revil (2012) also developed the following relationship between the quadrature conductivity and the specific surface area (in $\mathrm{kg\,m^{-2}}$) of the porous material

$$\sigma'' \approx -\frac{2}{3}\beta^S_{(+)} f \rho_g Q_S S_{Sp}, \tag{18}$$

where Q_S denotes the mean surface charge per unit surface area of the clay minerals (in $\mathrm{C\,m^{-2}}$) and S_{Sp} denotes the specific surface area (surface area per unit mass of the solid grains). Taking $\beta^S_{(+)}(25°\mathrm{C}, \mathrm{Na}^+) = 1.5\times10^{-10}\ \mathrm{m^2\,s^{-1}\,V^{-1}}$, $f = 0.90$, $Q_s = 0.32\ \mathrm{C\,m^{-2}}$ (Revil, 2012), $\rho_g = 2650\ \mathrm{kg\,m^{-3}}$, we have $\sigma'' \approx -aS_{Sp}$ with $a = 7.6\times10^{-8}\ \mathrm{S\,kg\,m^{-3}}$. This trend is shown in Figure 9 for clayey materials. In Figure 9, we have also reported the values of the quadrature conductivity for the saprolite core samples as a function of the specific surface area determined in Table 2 from the surface conductivity. The quadrature/specific surface area data are consistent with the clayey sand linear trend of the POLARIS induced polarization model developed recently by Revil (2012).

Using equations 12, 13, and 15, the expression of the phase and it critical value at low salinities (see Revil, 2012) are given by

$$\varphi = -\frac{\beta^S_{(+)} f Q_V}{\sigma_w + \beta_{(+)}(1-f)Q_V}, \tag{19}$$

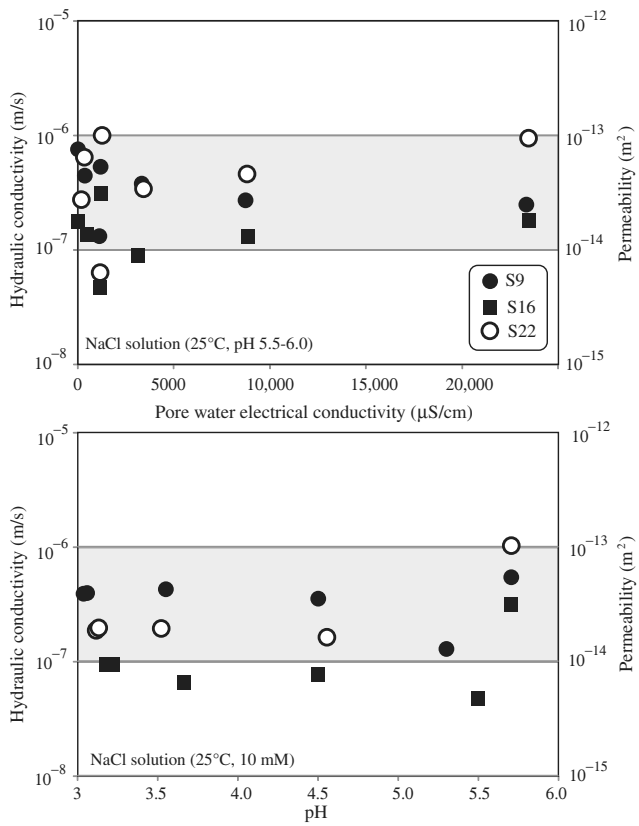

Figure 5. Measured saturated hydraulic conductivity or permeability versus the pore water conductivity and pH. Most of the measured values are between 10^{-7} and 10^{-6} $\mathrm{m\,s^{-1}}$. These laboratory data are consistent with the in situ measurements of the saturated hydraulic conductivity by McKay et al. (2005, KS-1 pit). The gray area corresponds to the range 10^{-6} to 10^{-7} $\mathrm{m\,s^{-1}}$.

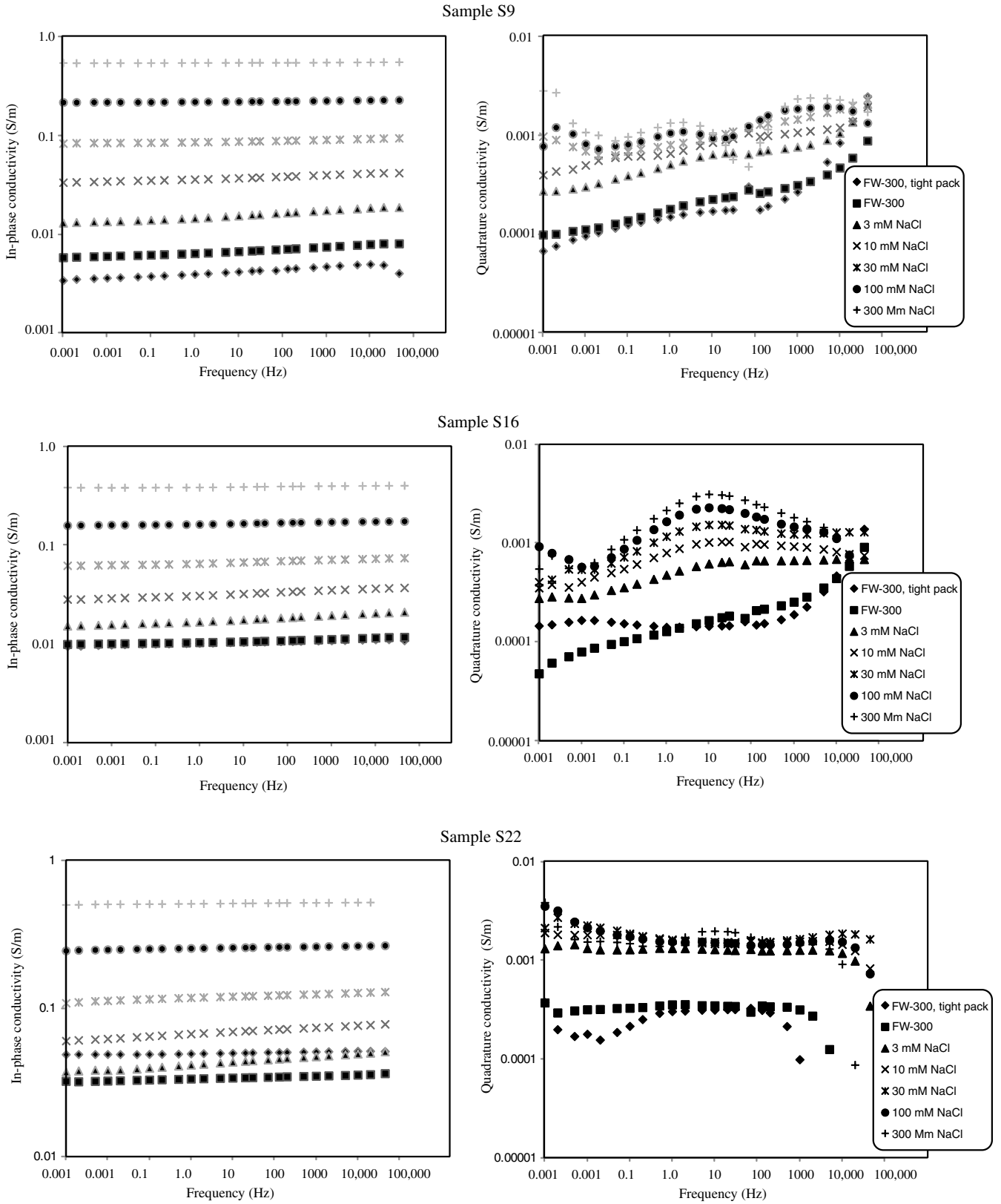

Figure 6. In-phase and quadrature conductivities at different pore water salinities. The pH values are in the range of 5–6.

Downloaded 01/22/13 to 138.67.207.132. Redistribution subject to SEG license or copyright; see Terms of Use at http://library.seg.org/

$$\lim_{\mathrm{Du}>>1} \varphi = -\frac{\beta^S_{(+)} f}{\beta_{(+)}(1-f)}. \tag{20}$$

This critical phase value is independent of the texture of the clayey material and is observed to be on the order of −30 mrad (see Vinegar and Waxman, 1984; Revil, 2012). This value of −30 mrad is consistent with taking $\beta^S_{(+)}(\mathrm{Na}^+) = 1.5 \times 10^{-10}\ \mathrm{m^2\,s^{-1}\,V^{-1}}$, $\beta_{(+)}(\mathrm{Na}^+) = 5.2 \times 10^{-8}\ \mathrm{m^2\,s^{-1}\,V^{-1}}$, and $f = 0.91$ in equation 20. In Figure 10, we plotted the phase lag data for the three samples and we determined the mean value of f and the mean value of Q_V. We obtained $f = 0.924 \pm 0.004$ and $Q_V = (5.7 \pm 0.9) \times 10^7\ \mathrm{C\,m^{-3}}$. The value of f is fairly consistent with the default value given by Revil (2012) for clayey materials ($f = 0.90$). The value of Q_V is consistent with the value given above ($3.1 \times 10^7\ \mathrm{C\,m^{-3}}$, determined using the CEC value of Kim et al. [2009] and the value of the porosity, see the discussion above). The value $f = 0.92$ is used in turn in Table 2 with the formation factor and surface conductivity data to determine the value of the CEC for each sample. Note that the CEC estimates determined in Table 2 from the surface conductivity data (in the range 1.4 to 12 cmol kg^{-1}) are grossly consistent with the CEC measurement of Kim et al. (2009) (10.5 cmol kg^{-1}).

We can also use the model developed by Revil (2012) to investigate the salinity dependence of the quadrature conductivity. In this model, the salinity dependence of the quadrature conductivity is coming from the salinity dependence of the partition coefficient f, which is given by

$$f = f_{\mathrm{M}} \left[\frac{\left(\frac{K_{\mathrm{Na}}}{10^{-\mathrm{pH}}(1-f_M)} \right) C_f}{1 + \left(\frac{K_{\mathrm{Na}}}{10^{-\mathrm{pH}}(1-f_M)} \right) C_f} \right], \tag{21}$$

where f_M denotes the maximum value of the partition coefficient reached at high salinity, the value of the equilibrium constant for the sorption of sodium is approximately $K_{\mathrm{Na}} = (3.0 \pm 0.4) \times 10^{-4}$ (Revil, 2012), and the pH is typically 6. Using the proportionality between the concentration and the electrical conductivity, we have

$$f = \frac{f_{\mathrm{M}} \sigma_w}{\frac{10^3 e N (\beta_{(+)} + \beta_{(-)}) 10^{-\mathrm{pH}} (1-f_M)}{K_{\mathrm{Na}}} + \sigma_w}, \tag{22}$$

where e represents the elementary charge (1.6×10^{-19} C) and N is the Avogadro number (6.02×10^{23} Mol^{-1}). Combining equation 22 with equation 15 and adding an additional contribution due to mobile protons along the mineral surface σ''_H (Skold and Revil, 2011) yields

$$\sigma'' = -\frac{a\sigma_w}{b + \sigma_w} + c, \tag{23}$$

Table 6. Conductivity and phase lag data at 1 Hz for different pore fluid salinities.

Sample	Effluent σ_w (S m^{-1})	Effluent pH	σ' (S m^{-1})	σ'' (S m^{-1})	φ (mrad)
S9	4.95e-3	4.67	3.98e-3	−1.51e-4	−37.9
S9	4.95e-3	5.59	6.45e-3	−1.81e-4	−28.1
S9	3.82e-2	5.41	1.47e-2	−5.10e-4	−34.7
S9	1.21e-1	5.76	3.63e-2	−6.61e-4	−18.2
S9	3.23e-1	4.79	8.66e-2	−8.10e-4	−9.4
S9	8.73e-1	4.69	2.20e-1	−1.1e-3	−4.8
S9	2.33	4.61	5.5e-1	−1.3e-3	−2.5
S16	4.95e-3	4.67	1.02e-2	−1.41e-4	−13.8[14]
S16	5.80e-3	6.57	1.03e-2	−1.27e-4	−12.3[14]
S16	3.88e-2	5.97	1.67e-2	−4.74e-4	−28.4
S16	1.21e-1	5.82	3.07e-2	−7.96e-4	−25.9
S16	3.22e-1	5.73	6.49e-2	−1.16e-3	−17.9
S16	8.83e-1	5.81	1.63e-1	−1.65e-3	−10.2
S16	2.35	5.72	3.90e-01	−2.1e-3	−5.6
S22	9.53e-3	7.15	4.94e-2	−3.04e-4	−6.2[14]
S22	7.09e-3	7.03	3.34e-2	−3.56e-4	−10.6[14]
S22	4.01e-2	6.36	4.15e-2	−1.32e-3	−31.8
S22	1.22e-1	6.8	6.73e-2	−1.63e-3	−24.2
S22	3.27e-1	5.96	1.18e-1	−1.59e-3	−13.5
S22	8.79e-1	6.23	2.55e-1	−1.55e-3	−6.1
S22	2.34	6.03	5.1e-1	−1.6e-3	−3.1

[14]Not considered for the fit shown in Figure 10.

Downloaded 01/22/13 to 138.67.207.132. Redistribution subject to SEG license or copyright; see Terms of Use at http://library.seg.org/

Downloaded 01/22/13 to 138.67.207.132. Redistribution subject to SEG license or copyright; see Terms of Use at http://library.seg.org/

where the two constants a and b are given by

$$a = \frac{1}{F}\beta^{S}_{(+)} Q_V f_{\mathrm{M}}, \tag{24}$$

$$b = \frac{10^3 eN(\beta_{(+)} + \beta_{(-)})10^{-\mathrm{pH}}(1 - f_M)}{K_{\mathrm{Na}}}, \tag{25}$$

and

$$c = \sigma''_H. \tag{26}$$

A fit of equation 23 to the data of samples S9 and S22 is shown in Figure 11. For Sample S9, we obtain $a = (1.1 \pm 0.1)\times 10^{-3}$, $b = (8.0 \pm 3.3) \times 10^{-2}\ \mathrm{S\,m^{-1}}$, and $c = (1.06 \pm 0.30)\times 10^{-4}\ \mathrm{S\,m^{-1}}$. For Sample S16, we obtain $a = (2.0 \pm 0.2) \times 10^{-3}$, $b = (18.7 \pm 4.8) \times 10^{-2}\ \mathrm{S\,m^{-1}}$, and $c = (0.82 \pm 0.17) \times 10^{-4}\ \mathrm{S\,m^{-1}}$. The values of a and b can be compared with the predictions from equations 24 and 25. For Sample S9, taking $f_M = 0.92$ and $Q_V = 5.7 \times 10^7\ \mathrm{C\,m^{-3}}$ (both from Figure 10), $\beta^{S}_{(+)}(\mathrm{Na^+}) = 1.5 \times 10^{-10}\ \mathrm{m^2\,s^{-1}\,V^{-1}}$, and $F = 3.95$ (Table 2), yields $a = 2.0 \times 10^{-3}$, which compares quite well with $a = (1.1 \pm 0.1) \times 10^{-3}$ determined from the measurements. Taking the same values for Sample S16 but with $F = 5.9$ (Table 2), we obtain $a = (1.3 \pm 0.1) \times 10^{-3}$, which compare well with $a = (2.0 \pm 0.2) \times 10^{-3}$ determined from the measurements. For b, taking $K_{\mathrm{Na}} = 3.0 \times 10^{-4}$ and $\mathrm{pH} = 4.5$ in equation 25, we obtain $b = 10 \times 10^{-2}\ \mathrm{S\,m^{-1}}$ in fair agreement with the value given above {for S9, $b = (8.0 \pm 3.3) \times 10^{-2}\ \mathrm{S\,m^{-1}}$, and for S16, $b = (18.7 \pm 4.8) \times 10^{-2}\ \mathrm{S\,m^{-1}}$}. The quadrature conductivity associated with the protons seems quite constant and equal to $1.0 \times 10^{-4}\ \mathrm{S\,m^{-1}}$ for the two samples.

STREAMING POTENTIAL COUPLING COEFFICIENT

Streaming potential data from a typical experiment are shown at Figure 12. The differences of the electrical potential measured in the vicinity of the end faces of the core sample are proportional to the imposed hydraulic heads, indicating good measurements. The slope of the linear trend of streaming potential versus head corresponds to the streaming potential coupling coefficient (see equation 29).

The streaming current represents the quasistatic source current density associated with the drag of the excess of electrical charges in the electrical diffuse layer in porous material by the flow of the pore water. The streaming potential can be used in the field to characterize preferential groundwater flow paths (Wilt and Corwin, 1989; Wilt and Butler, 1990; Panthulu et al., 2001). The total (electromigration) current density is given for quasistatic conditions by (Revil et al., 2011)

$$\mathbf{J} = \sigma_0 \mathbf{E} + \hat{Q}_V \mathbf{u}, \tag{27}$$

where $\hat{Q}_V$ represent the effective (excess) charge of the diffuse layer that can be dragged by the pore water flow, $\mathbf{E}$ denotes the electrical

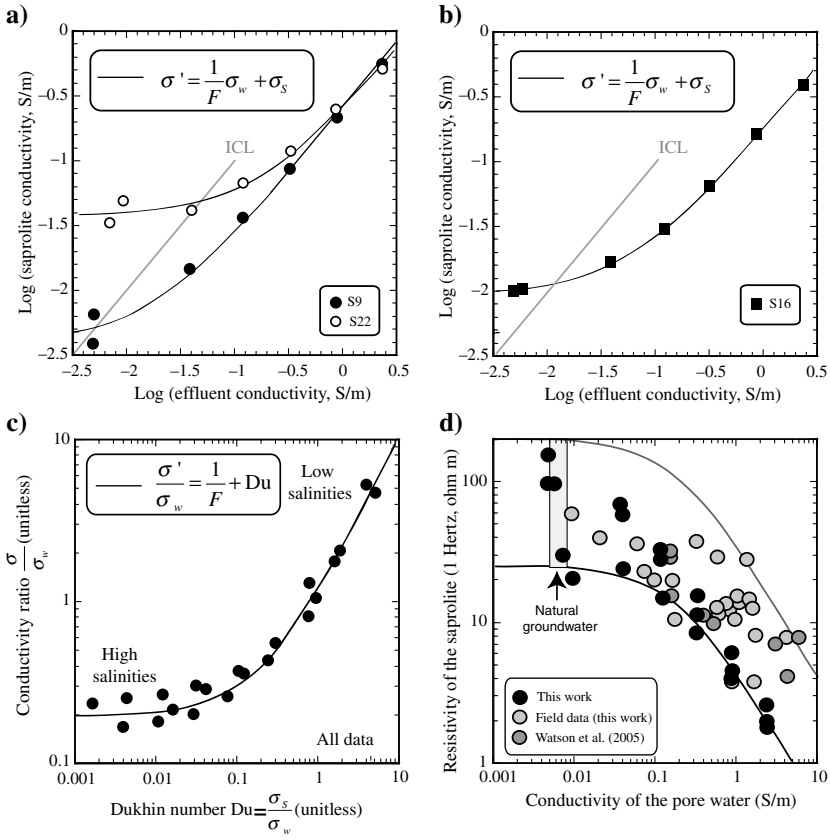

Figure 7. Analysis of the in-phase conductivity data. (a, b) In-phase electrical conductivity of the saprolite versus the conductivity of the effluent taken as a proxy for the pore water conductivity (measurement at 1 H). (c) Normalization of the data set. The ICL represents the isoconductivity line for which the conductivity of the core sample is equal to the pore water conductivity. Therefore, the three core samples have an isoconductivity point. (d) Field data from Watson et al. (2005) and Revil et al. (2012). The field data indicate a formation factor in the range of 5–40 and the same magnitude for the surface conductivity shown by the laboratory data.

Downloaded 01/22/13 to 138.67.207.132. Redistribution subject to SEG license or copyright; see Terms of Use at http://library.seg.org/

field (V m^{-1}), and σ_0 is the DC conductivity. The last term of equation 27 can be obtained easily by volume averaging the local current density in the pore space $\mathbf{j}_S = \rho\mathbf{v}$, where ρ denotes the local charge density and $\mathbf{v}$ is the local velocity. The (volumetric) charge density $\hat{Q}_V$ is expected to be only a fraction of the diffuse layer volumetric charge density given by

$$\bar{Q}_V = (1 - f)Q_V, \tag{28}$$

(Revil and Florsch, 2010; Jougnot et al., 2012). Using $Q_V = 4.0 \times 10^7$ C m^{-3} and $f = 0.9$ yields $\bar{Q}_V = 4 \times 10^6$ C m^{-3}. Therefore, $\hat{Q}_V$ represents only a very small fraction of this value.

We use Darcy's law, equation 1, to express in equation 27 the Darcy velocity $\mathbf{u}$ as a function of the hydraulic head h. This yields the following expression for the total current density:

$$\mathbf{J} = -\sigma_0 \nabla\psi - K\hat{Q}_V \nabla h, \tag{29}$$

where h denotes the hydraulic head (in m), σ_0 is the DC conductivity (in S m^{-1}), and ψ is the streaming potential (in V). The streaming potential coupling coefficient is defined by (see Helmholtz, 1879)

$$C \equiv \left(\frac{\partial\psi}{\partial h}\right)_{\mathbf{J}=0}, \tag{30}$$

where we have used the hydraulic head instead of the fluid pressure in the classical definition found in the literature. This coupling coefficient characterizes the sensitivity of the electrical potential, in this case called the "streaming potential," to the hydraulic head. It can be determine directly from the streaming potential data reported versus the hydraulic heads (so it corresponds to the slope of the trends shown in Figure 12). From equations 29 and 30, this coefficient is given by (Bolève et al., 2007a, 2007b; Revil et al., 2010)

$$C = -\frac{K\hat{Q}_V}{\sigma_0}. \tag{31}$$

Equation 31 is used to determine the effective volumetric charge density $\hat{Q}_V$ from the measurements of the streaming potential coupling coefficient C, hydraulic conductivity, and DC electrical conductivity. Using equations 8 and 31, the coupling coefficient is related to the pore water conductivity as

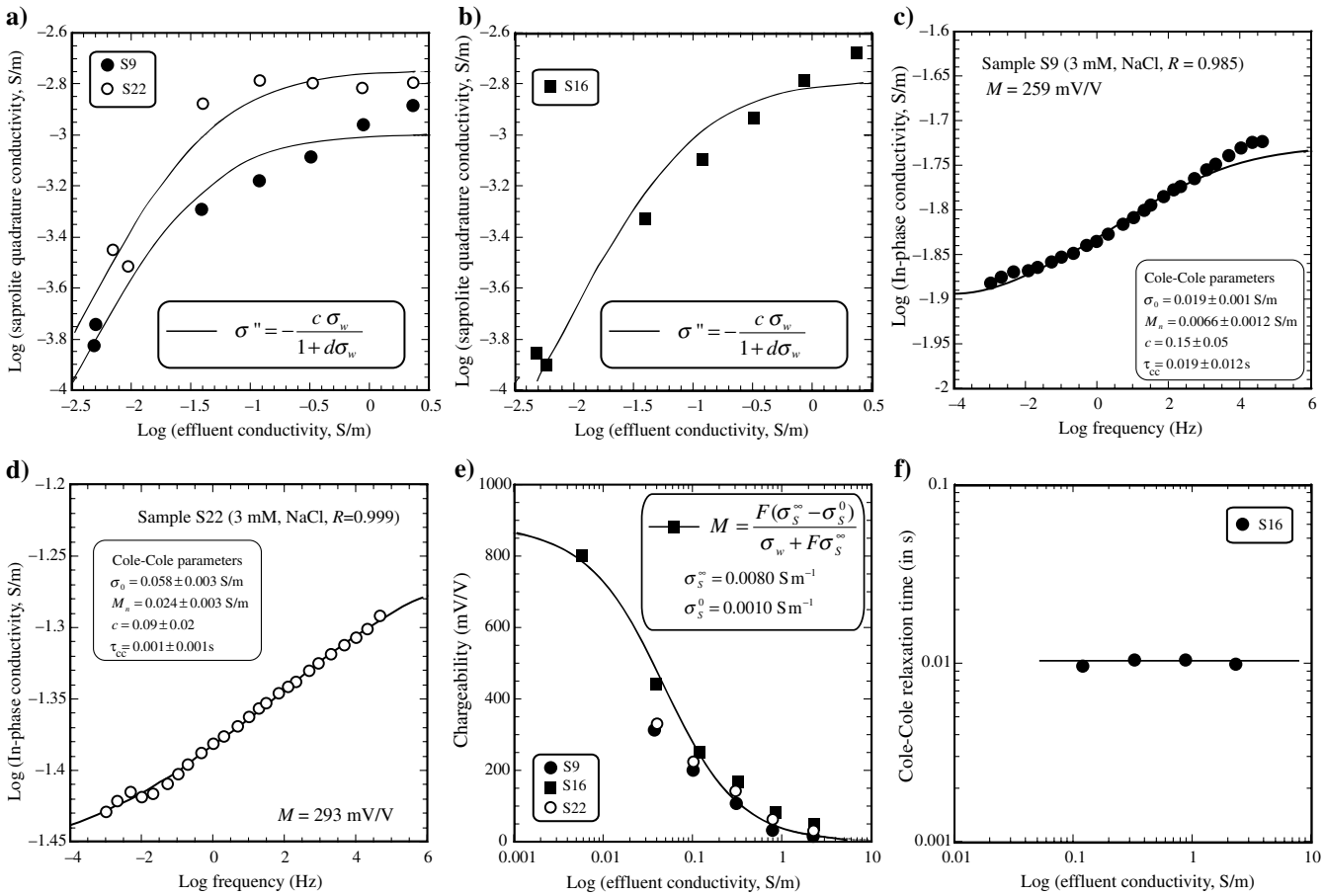

Figure 8. Induced polarization parameters. (a, b) Quadrature electrical conductivity of the saprolite versus the conductivity of the effluent taken as a proxy for the pore water conductivity (measurement at 1 H). (c) (d) Determination of the chargeability by fitting a Cole-Cole model to the in-phase conductivity data. (e) Chargeability versus pore water conductivity. (f) Cole-Cole relaxation time (in s) for conductivity versus the pore water conductivity (in S m^{-1}).

$$C = -\frac{FK\hat{Q}_V}{\sigma_w + F\sigma_S}. \tag{32}$$

The streaming potential coupling coefficient is the fundamental petrophysical parameter characterizing the magnitude of streaming potentials in the field. This equation can be used to see if we can predict the coupling coefficient.

An alternative approach to describe the streaming potential coupling coefficient is to use the zeta potential ζ (Merkler et al., 1989; Pengra et al., 1999; Leroy et al., 2004; Leroy and Revil, 2009). In this case, the expression for the streaming potential coupling coefficient becomes

$$C = -\frac{\varepsilon_w \rho_w g \zeta}{\eta_w(\sigma_w + F\sigma_S)}, \tag{33}$$

where ρ_w denotes the mass density of the pore water, g is the gravitational acceleration (9.81 m s^{-2}), and ε_w denotes the dielectric constant of the pore water ($81 \times 8.84 \times 10^{-12}$ F m^{-1}). Equation 33 is a variant of the so-called Helmholtz-Smoluchowski equation (Helmholtz, 1879), which is usually given without the surface conductivity term ($C_{HS} = -\varepsilon_w \rho_w g \zeta / \eta_w \sigma_w$ or $C_{HS} = -\varepsilon_w \zeta / \eta_w \sigma_w$ if the head is expressed in pore fluid pressure; see Bolève et al., 2007b).

The streaming potential coupling coefficient was determined for the three samples at NaCl concentrations ranging from 3 to

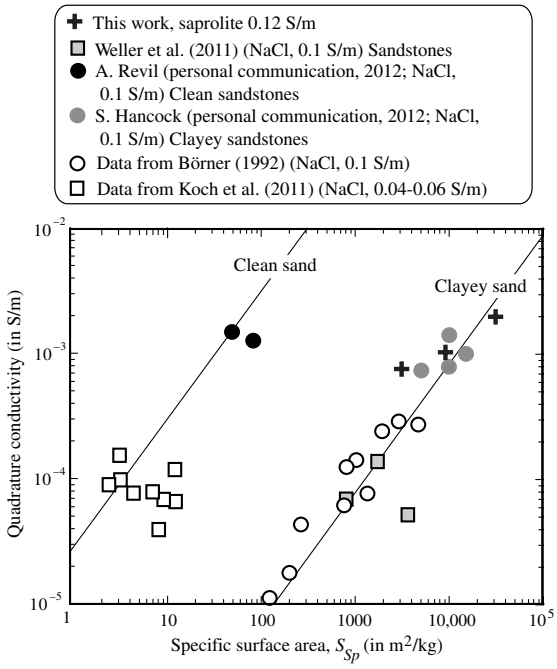

Figure 9. Influence of the specific surface area S_{Sp} upon the quadrature conductivity. We observe that the saprolite samples are characterized by relatively high specific surface areas and high quadrature conductivities in agreement with the trend determined for clayey sands by Revil (2012). Data are from Börner (1992), Koch et al. (2011), Weller et al. (2011), and S. Hancock (personal communication, 2012). For the saprolite, the values are taken at 10 H and the CEC are from Table 1 (from surface conductivity).

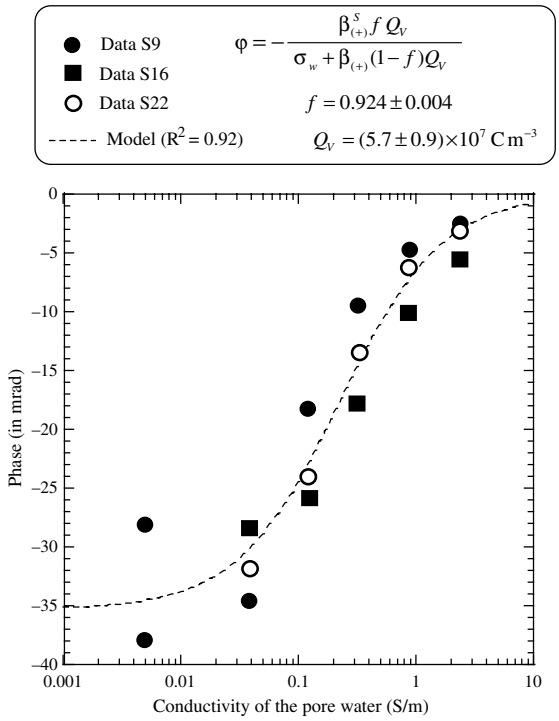

Figure 10. Determination of the partition coefficient f (fraction of the counterions in the Stern layer) and total volumetric charge density Q_V using the phase lag data plotted as a function of the conductivity of the pore water (at 1 H, NaCl). The dashed line corresponds to the best fit of the model.

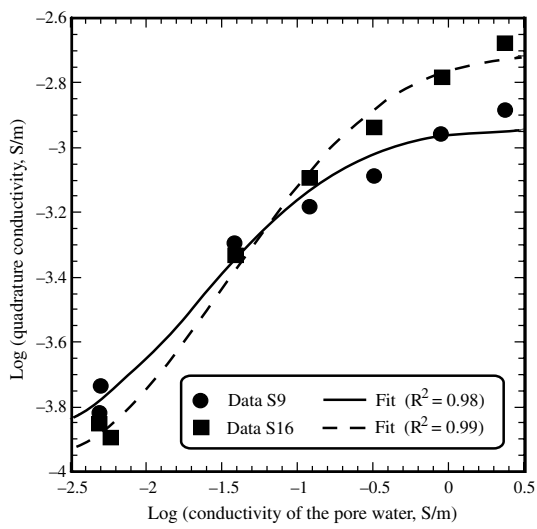

Figure 11. Quadrature conductivity versus pore water electrical conductivity. The plain and dashed lines correspond to the best least-squares fit of equation 23 of the main text. Note the sigmoid shape of the trends indicating the existence of a low-salinity asymptotic limit (associated with mobile protons) and a high salinity limit associated with the sorption of sodium on the mineral surface.

Downloaded 01/22/13 to 138.67.207.132. Redistribution subject to SEG license or copyright; see Terms of Use at http://library.seg.org/

Downloaded 01/22/13 to 138.67.207.132. Redistribution subject to SEG license or copyright; see Terms of Use at http://library.seg.org/

300 mM. In Figure 13, we report the value of the streaming potential coupling coefficient as a function of the conductivity of the pore water. We fit a function of the form

$$C = -\frac{a}{\sigma_w + b}, \tag{34}$$

and once a is determined, the value of the effective charge density is determined by $\hat{Q}_V = a/FK$. The results are reported in Table 2. The volumetric charge density $\hat{Q}_V$ is in the range of 140–490 C m^{-3}, which represents therefore only a small fraction of the total charge density of the diffuse layer ($\bar{Q}_V = 4 \times 10^6$ C m^{-3}), which is consistent with the results reported recently by Jougnot et al. (2012). The estimates for the effective charge per unit pore volume are compared with other literature data in Figure 14. Like for other natural porous materials at near-neutral pH values, the effective charge per unit pore volume $\hat{Q}_V$ is controlled by the value of the permeability of the material.

We use equation 33 to determine the values of the zeta potential for each core sample at the different pore water conductivities. We use the values of the surface conductivities and formation factors reported in Table 2. The results are shown in Figure 15. The zeta potential is in the range of −10 to −20 mV and seems independent of the conductivity of the pore water.

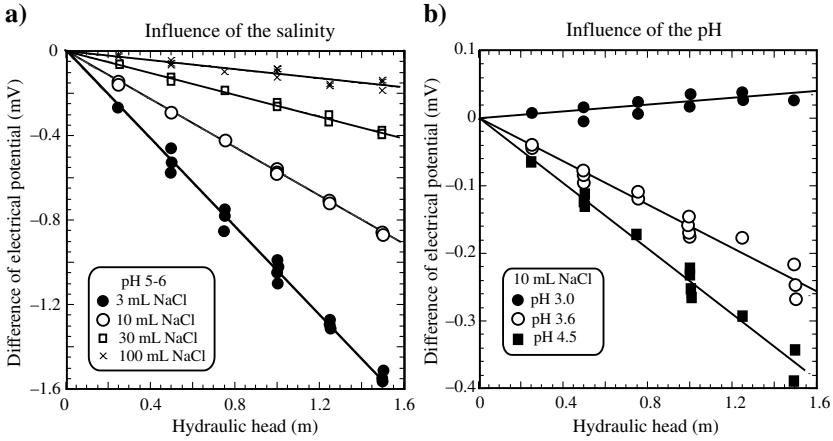

Figure 12. Example of the measurement of the streaming potential for various values of the hydraulic head (a) Influence of the salinity various salinities (NaCl solutions, Sample S16). (b) Influence of the pH (NaCl solution 10 mM, Sample S9). Note that at pH 3, the coupling coefficient is positive and hence the zeta potential is positive. This indicates that the isoelectric point is between pH 3.6 and 3.0.

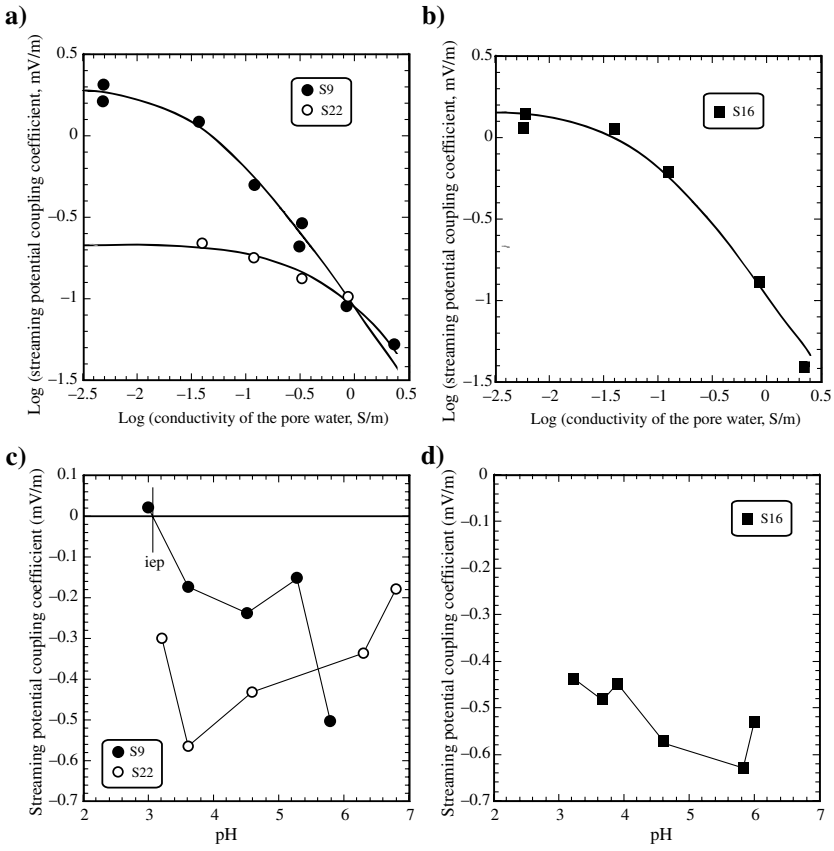

Figure 13. Streaming potential coupling coefficient. (a, b) Value of the streaming potential coupling coefficient (negative) versus the pore water conductivity (NaCl solutions, pH ≈ 6). The plain lines correspond to the fit of the data with a function $C = a/(\sigma_f + b)$. Sample S22 is influenced by the presence of the smectite, which is generating high surface conductivity and therefore a smaller value of the magnitude of the streaming potential coupling coefficient at low salinities. The term "iep" stands for the isoelectric point. (c, d) Value of the streaming potential coupling coefficient versus the pH (NaCl solutions, σ_w in the range 0.12–0.16 S m^{-1}).

Downloaded 01/22/13 to 138.67.207.132. Redistribution subject to SEG license or copyright; see Terms of Use at http://library.seg.org/

INFLUENCE OF THE PH

The previous analysis was done with keeping the pH at relatively high values (in the range of 5.5–7.0). Do these petrophysical properties represent the saprolite near the S-3 ponds, which have been bathed in acid for a few decades? To partially reply to this question, we have also performed additional investigations to look at the effect of the pH (in the range of 3 to 6) on these petrophysical properties.

The pH dependence of the hydraulic conductivity is shown in Figure 5. It seems that there is no pH dependence of the hydraulic conductivity with the pH, which may indicate that there is no dissolution during our experiments (over a two-month period). The pH dependence of the streaming potential coupling coefficient is shown in Figure 13 and reported in Table 7. Samples S9 and S16 have an isoelectric point at a pH close to 3 (the isoelectric point corresponds to the value of the pH for which the zeta potential is equal to zero). We observe that Sample S22 shows a different behavior, but the data are noisier.

We analyzed the in-phase and quadrature conductivity data as a function of the pH. The spectra are shown in Figure 16, and the in-phase and quadrature conductivities are shown in Figure 17 versus the pH at 1 H. We see that the in-phase and quadrature conductivities are pH dependent but the correlation between the pH and the conductivities is not clear. The surface conductivity (see the gray area in the first column of Figure 17) is highly pH dependent and is nearly zero at the isoelectric points for Samples S9. This is consistent with the POLARIS model of Revil (2012), in which the surface conductivity is dominated by the diffuse layer and the quadrature conductivity by the Stern layer. A possibility is that the surface conductivity is therefore expected to be zero at the isoelectric point at which the diffuse layer disappears (Sample S9). We see that the quadrature conductivity is not going to zero for all the samples. This is consistent with the fact that there are still some counterions in the Stern layer at the isoelectric point, which would explain why the quadrature conductivity is not equal to zero at the isoelectric point.

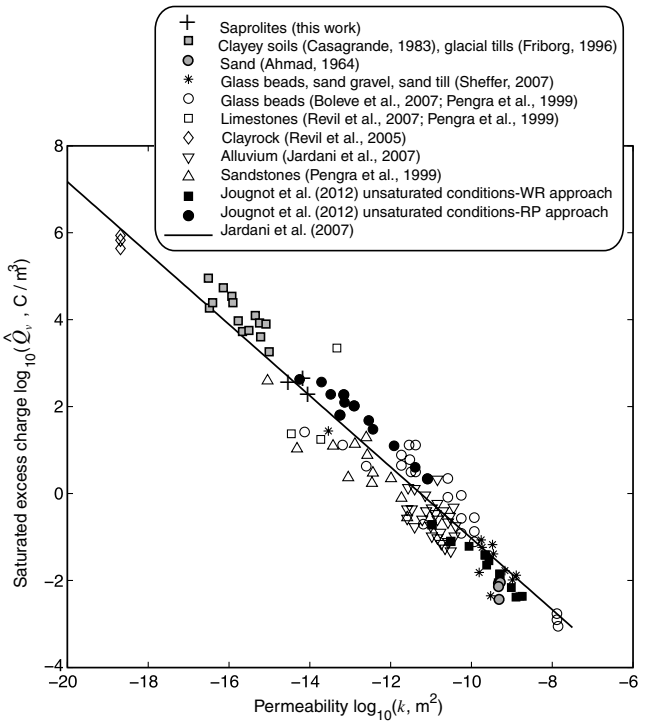

Figure 14. Effective excess of electrical charges movable by the pore water flow versus permeability for a broad collection of core samples near neutral pH conditions (5 to 8). Data are from Ahmad (1964), Casagrande (1983), Friborg (1996), Pendra et al. (1999), Revil et al. (2005, 2007), Bolève et al. (2007b), Jardani et al. (2007), Sheffer (2007), and Jougnot et al. (2012).

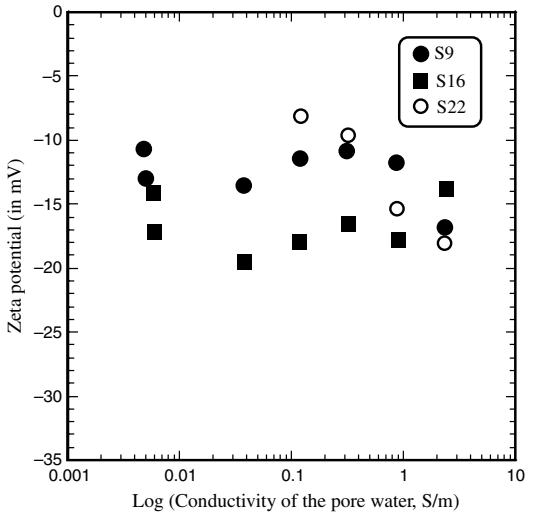

Figure 15. Estimation of the zeta potential of the three core samples. The zeta potential appears relatively independent of the pore water conductivity and suggests a constant zeta potential for the saprolite.

Table 7. Influence of the pH upon the streaming potential coupling coefficient *C* (25°C, NaCl 10 mM).

pH	Sample	Effluent	*C*
		σ_w (S m^{-1})	(mV/m)
5.8	S9	0.121	−0.5
5.3	S9	0.118	−0.15
4.5	S9	0.119	−0.24
3.6	S9	0.118	−0.17
3.0	S9	0.162	0.02
6.0	S16	0.120	−0.53
5.8	S16	0.121	−0.63
4.6	S16	0.120	−0.57
3.9	S16	0.116	−0.45
3.0	S16	0.145	−0.02
6.8	S22	0.122	−0.18
6.3	S22	0.119	−0.34
4.6	S22	0.120	−0.43
3.6	S22	0.120	−0.56
3.2	S22	0.152	−0.3

For Samples S16 and S22, the streaming coupling coefficient shown in Figure 13c and 13d does not exhibit an isoelectric point and the surface conductivity remains high at low pH values. We know that smectite exhibits such behavior. Indeed, according to Kriaa et al. (2009), the layers of smectite have a permanent negative charge associated with isomorphic substitutions in the crystalline framework (Figure 4). They have also pH-dependent charges on the edge of their crystals due to the presence of hydroxyl sites. The point of zero charge of these amphoteric edges sites is, however, in the range of ~7.5–9.3, so it is above the pH range investigated in the present work. The observed dependence of the zeta potential with the pH of the saprolite could be due to a mixed influence of the surface properties of silica, illite, and smectite depending on the clay composition of the material. Therefore, there is an incentive to pursue this work using a broader database of core samples.

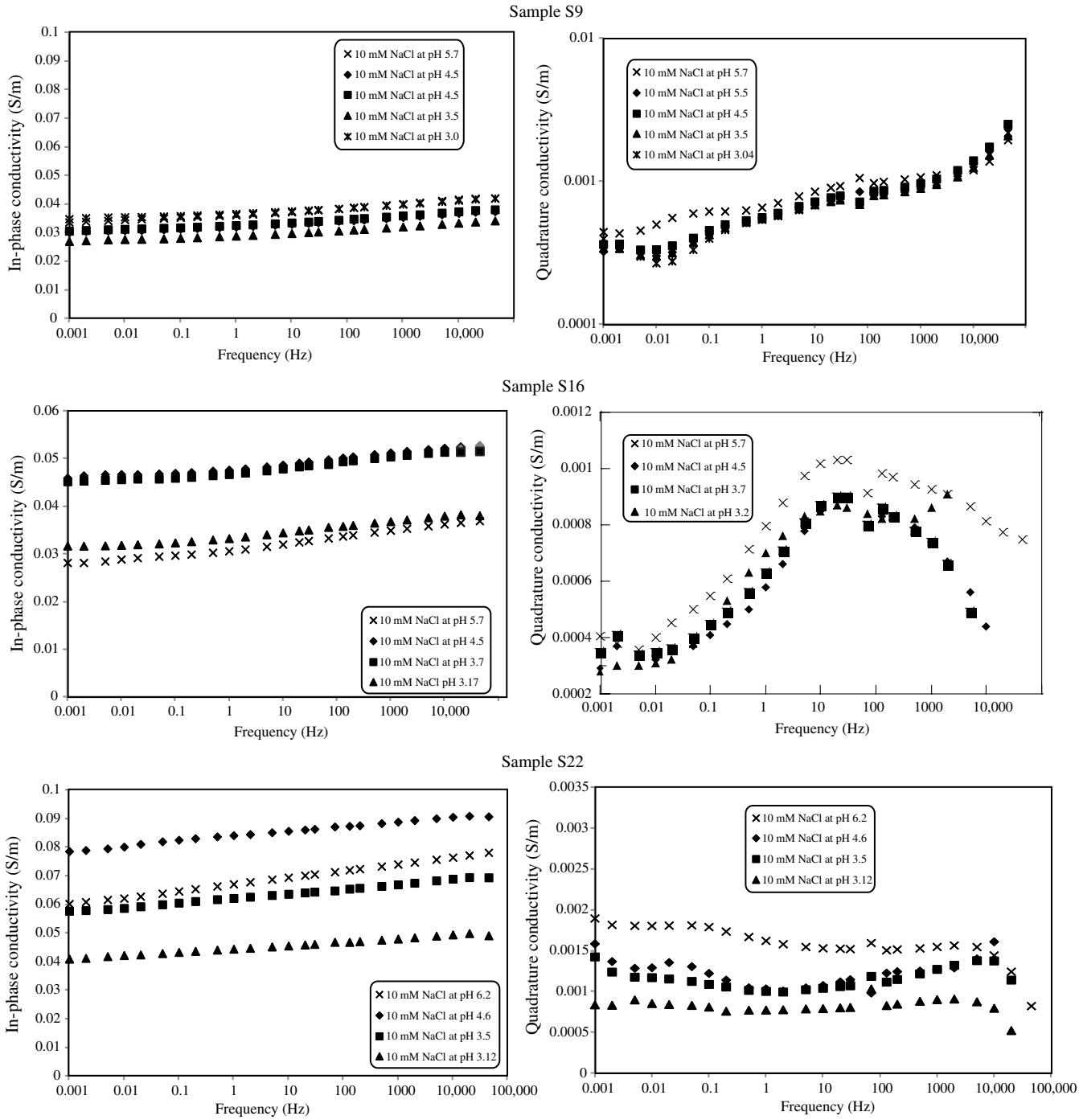

Figure 16. In-phase and quadrature conductivities at different pH values (NaCl, 10 mM). All the measurements are performed at equilibrium (the pH of the effluent is equal to the pH of the influent).

Downloaded 01/22/13 to 138.67.207.132. Redistribution subject to SEG license or copyright; see Terms of Use at http://library.seg.org/

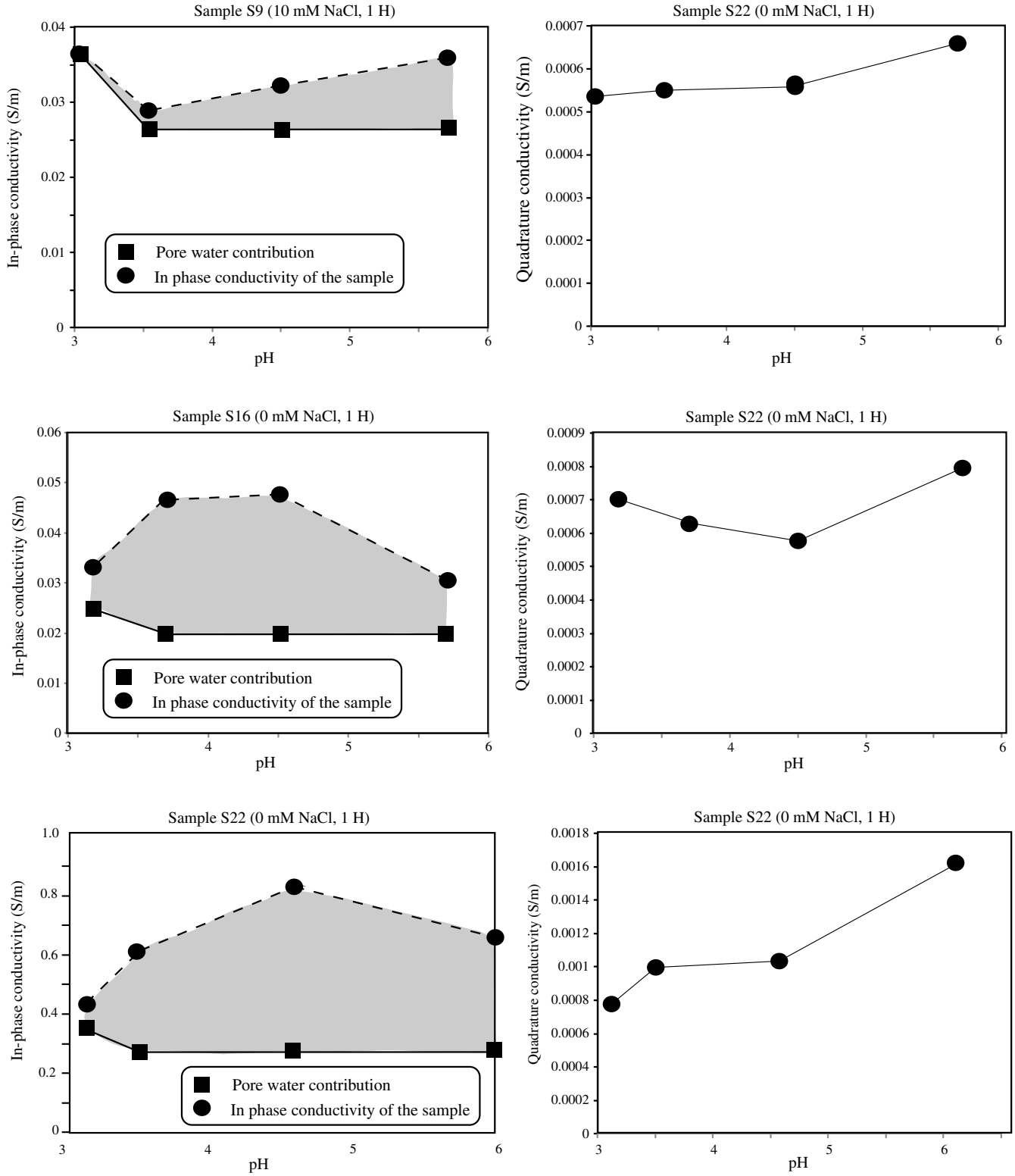

Figure 17. Influence of the pH upon the in-phase and quadrature conductivity components of the complex conductivity of the saprolite. The gray area corresponds to the surface conductivity determined from equation 12 and the data. The surface conductivity corresponds to the difference between the in-phase conductivity and the contribution of the pore water conductivity σ_w/F, where σ_w denotes the measured pore water (effluent) conductivity and F is taken from Table 2 (except for Sample S9 for which we use a slightly higher value, 4.5 instead of 4.1, to insure a positive surface conductivity).

Downloaded 01/22/13 to 138.67.207.132. Redistribution subject to SEG license or copyright; see Terms of Use at http://library.seg.org/

Downloaded 01/22/13 to 138.67.207.132. Redistribution subject to SEG license or copyright; see Terms of Use at http://library.seg.org/

CONCLUSIONS

We have documented the permeability, the complex conductivity, and the streaming potential coupling coefficient of three saprolite samples collected from the IFRC background location at Oak Ridge. Regarding the petrophysical data gathered in this study and their interpretation in terms of a physics-based model, the following conclusions have been reached:

- The hydraulic conductivity of the core samples ranges between 10^{-7} and 10^{-6} m s^{-1} in agreement with field observations.
- For electrical conductivity measurements, the cementation exponent is equal to 2.2 ± 0.3 and the surface conductivity at 25°C ranges between 4×10^{-3} S m^{-1} (Sample S9) and 38×10^{-3} S m^{-1} (Sample S22) depending on the alteration of the material. The core samples show the existence of an isoconductivity point at low pore water conductivity (at this point, the conductivity of the saprolite is equal to the conductivity of the pore water). The surface conductivity is dominated by electromigration in the electrical diffuse layer coating the pore water/mineral interface.
- The streaming potential coupling coefficient is in agreement with recent models. At high salinities, the streaming potential coupling coefficient is inversely proportional to the pore water conductivity, while at very low salinities, the streaming potential coupling coefficient is controlled by the surface conductivity and is therefore smaller for highly weathered samples containing mixed layer illite-smectite and smectite clays. The samples with the highest amount of smectite (S16 and S22) keep a high surface conductivity including at low pH values, possibly because of the high level of isomorphic substitutions in the crystalline framework.
- For all the samples, the quadrature conductivity is weakly pH dependent. This proves clearly that the quadrature conductivity (hence the polarization) is not controlled by the diffuse layer but more likely by the Stern layer. The quadrature conductivity/CEC data (the CEC being determined by the in-phase surface conductivity) implies a mobility of the counterions in the Stern layer two orders of magnitude smaller than in the diffuse layer.

The petrophysical properties determined from laboratory experiments presented in this work will be used in a subsequent study to interpret geophysical surveying (3D resistivity tomography, time-lapse 2D DC resistivity, time-domain induced polarization data, and self-potential measurements) performed around the former S-3 ponds. The geoelectrical data, interpreted using the petrophysical model tested here, are expected to be useful at this key DOE contaminated site for locating preferential fluid flow pathways and for investigating the 3D geometry of the contaminant plumes near the former S-3 ponds.

ACKNOWLEDGMENTS

We thank the Environment Remediation Science Program (ERSP), U. S. Department of Energy (DOE), for the funding (award DE-FG02-08ER646559), Richard Wendlandt for XRD analysis, and Manika Prasad for the specific surface area (BET) measurements. We thank Egon Zimmerman for the quality of his impedance meter. We also thank Evert Slob and three anonymous referees for their very constructive reviews.

REFERENCES

Ahmad, M. U., 1964, A laboratory study of streaming potentials: Geophysical Prospecting, **12**, 49–64, doi: 10.1111/j.1365-2478.1964.tb01889.x.

Archie, G. E., 1942, The electrical resistivity log as an aid in determining some reservoir characteristics: Transactions of the American Institute of Mining, Metallurgical, and Petroleum Engineers, **146**, 54–62.

Bolève, A., A. Crespy, A. Revil, F. Janod, and J. L. Mattiuzzo, 2007a, Streaming potentials of granular media: Influence of the Dukhin and Reynolds numbers: Journal of Geophysical Research, **112**, B08204, doi: 10.1029/2006JB004673.

Bolève, A., A. Revil, F. Janod, J. L. Mattiuzzo, and A. Jardani, 2007b, Forward modeling and validation of a new formulation to compute self-potential signals associated with ground water flow: Hydrology and Earth System Sciences, **11**, 1661–1671, doi: 10.5194/hess-11-1661-2007.

Börner, F. D., 1992, Complex conductivity measurements of reservoir properties, *in* Proceedings of the third European core analysis symposium, Paris: Society of Core Analysts, 359–386.

Brunauer, S., P. Emmett, and E. Teller, 1938, Adsorption of gases in multimolecular layers: Journal of American Chemical Society, **60**, 309–319, doi: 10.1021/ja01269a023.

Casagrande, L., 1983, Stabilization of soils by means of electro-osmosis: State of the art: Journal of Boston Society of Civil Engineers, **69**, 255–302.

Chen, J., S. S. Hubbard, V. Korneev, D. Gaines, G. Baker, and D. Watson, 2010, Stochastic inversion of seismic refraction data for estimating watershed-scale aquifer geometry: development and application to a contaminated aquifer: Water Resources Research, **46**, W11539, doi: 10.1029/2009WR008715.

Chen, J., S. S. Hubbard, J. Peterson, K. Williams, M. Fienen, P. Jardine, and D. Watson, 2006, Development of a joint hydrogeophysical inversion approach and application to a contaminated fractured aquifer: Water Resources Research, **42**, W06425, doi: 10.1029/2005WR004694.

Cole, K. S., and R. H. Cole, 1941, Dispersion and absorption in dielectrics I. Alternating current characteristics: Journal of Chemical Physics, **9**, 341–351, doi: 10.1063/1.1750906.

Darcy, H., 1856, Les fontaines publiques de la Ville de Dijon: Dalmont.

Driese, S. G., 2002, Report on petrographic and geochemical characterization of Nolichucky shale saprolite, Cores FB300 and FB301, NABIR Field Site, Oak Ridge reservation: DOE report, http://public.ornl.gov/orifc/other/Petographicrpt.pdf.

Driese, S. G., L. D. McKay, and C. P. Penfield, 2001, Lithologic and pedogenic influences on porosity distribution and groundwater flow in fractured sedimentary saprolite: A new application of environmental sedimentology: Journal of Sedimentary Research, **71**, 843–857, doi: 10.1306/2DC4096D-0E47-11D7-8643000102C1865D.

Dueck, G., and T. Scheuer, 1990, Threshold accepting: A general purpose optimization algorithm appearing superior to simulated annealing: Journal of Computational Physics, **90**, 161–175, doi: 10.1016/0021-9991(90)90201-B.

Dukhin, S. S., and V. N. Shilov, 2002, Non-equilibrium electrical surface phenomena and extended electrokinetic characterization of particles, *in* A. V. Delgado, ed., Interfacial electrokinetics and electrophoresis: Surfactant science series **106**, CRC, 55–85.

Friborg, J., 1996, Experimental and theoretical investigations into the streaming potential phenomenon with special reference to applications in glaciated terrain: Ph.D. thesis, Lulea University of Technology.

Gasperikova, E., S. S. Hubbard, D. B. Watson, G. S. Baker, J. E. Peterson, M. B. Kowalsky, M. Smith, and S. Brooks, 2012, Long-term electrical resistivity monitoring of recharge-induced contaminant plume behavior: Journal of Contaminant Hydrology, **142–143**, 33–49, doi: 10.1016/j.jconhyd.2012.09.007.

Gu, B., S. C. Brooks, Y. Roh, and P. M. Jardine, 2003, Geochemical reaction and dynamics during titration of a contaminated groundwater with high uranium, aluminum, and calcium: Geochimica et Cosmochimica Acta, **67**, 2749–2761, doi: 10.1016/S0016-7037(03)00097-8.

Helmholtz, H., 1879, Study concerning electrical boundary layers: Weidemann Annal Physik Chemie, **7**, 337–382, 3rd edition.

Jardani, A., A. Revil, A. Bolève, J. P. Dupont, W. Barrash, and B. Malama, 2007, Tomography of groundwater flow from self-potential (SP) data: Geophysical Research Letters, **34**, L24403, doi: 10.1029/2007GL031907.

Jardine, P. M., G. K. Jacobs, and J. D. O'Dell, 1993b, Unsaturated transport processes in undisturbed heterogeneous porous media II. Co-contaminants: Soil Science Society of America Journal, **57**, 954–962, doi: 10.2136/sssaj1993.03615995005700040013x.

Jardine, P. M., G. K. Jacobs, and G. V. Wilson, 1993a, Unsaturated transport processes in undisturbed heterogeneous porous media. I. Inorganic contaminants: Soil Science Society of America Journal, **57**, 945–953, doi: 10.2136/sssaj1993.03615995005700040012x.

Jardine, P. M., G. V. Wilson, and R. J. Luxmoore, 1988, Modeling the transport of inorganic ions through undisturbed soil columns from two contrasting

watersheds: Soil Science Society of America Journal, **52**, 1252–1259, doi: 10.2136/sssaj1988.03615995005200050007x.
Jougnot, D., A. Ghorbani, A. Revil, P. Leroy, and P. Cosenza, 2010, Spectral induced polarization of partially saturated clay-rocks: A mechanistic approach: Geophysical Journal International, **180**, 210–224, doi: 10.1111/j.1365-246X.2009.04426.x.
Jougnot, D., N. Linde, A. Revil, and C. Doussan, 2012, Derivation of soil-specific streaming potential electrical parameters from hydrodynamic characteristics of partially saturated soils: Vadoze Zone Journal, **11**, doi: 10.2136/vzj2011.0086.
Kim, Y. J., J. W. Moon, Y. Roh, and S. C. Brooks, 2009, Mineralogical characterization of saprolite at the FRC background site in Oak Ridge, Tennessee: Environmental Geology, **58**, 1301–1307, doi: 10.1007/s00254-008-1633-1.
Koch, K., A. Kemna, J. Irving, and K. Holliger, 2011, Impact of changes in grain size and pore space on the hydraulic conductivity and spectral induced polarization response of sand: Hydrology and Earth System Sciences, **15**, 1785–1794, doi: 10.5194/hess-15-1785-2011.
Kooner, Z. S., P. M. Jardine, and S. Feldman, 1995, Competitive surface complexation reactions of SO_4^{2-} and natural organic carbon on soil: Journal of Environmental Quality, **24**, 656–662, doi: 10.2134/jeq1995.00472425002400040016x.
Kowalsky, M. B., E. Gasperikova, S. Finsterle, D. Watson, G. Baker, and S. S. Hubbard, 2011, Coupled modeling of hydrogeochemical and electrical resistivity data for exploring the impact of recharge on subsurface contamination: Water Resources Research, **47**, W02509, doi: 10.1029/2009WR008947.
Kriaa, A., N. Hamdi, and E. Srasra, 2009, Proton adsorption and acid-base properties of Tunisian illites in aqueous solution: Journal of Structural Chemistry, **50**, 273–287, doi: 10.1007/s10947-009-0039-6.
Leroy, P., and A. Revil, 2004, A triple layer model of the surface electrochemical properties of clay minerals: Journal of Colloid and Interface Science, **270**, 371–380, doi: 10.1016/j.jcis.2003.08.007.
Leroy, P., and A. Revil, 2009, Spectral induced polarization of clays and clay-rocks: Journal of Geophysical Research, **114**, B10202, doi: 10.1029/2008JB006114.
Leroy, P., A. Revil, A. Kemna, P. Cosenza, and A. Gorbani, 2008, Spectral induced polarization of water-saturated packs of glass beads: Journal of Colloid and Interface Science, **321**, 103–117, doi: 10.1016/j.jcis.2007.12.031.
Lipsicas, M., 1984, Molecular and surface interactions in clay intercalates, *in* D. L. Johnson, and P. N. Sen, eds., Physics and chemistry of porous media: American Institute of Physics, 191–202.
McKay, L. D., S. G. Driese, K. H. Smith, and M. J. Vepraskas, 2005, Hydrogeology and pedology of saprolite formed from sedimentary rock, eastern Tennessee, USA: Geoderma, **126**, 27–45.
Merkler, G.-P., H. Militzer, H. Hötzl, H. Armbruster, and J. Brauns, 1989, Detection of subsurface flow phenomena: **27**, Springer.
Olhoeft, G. R., 1985, Low-frequency electrical properties: Geophysics, **50**, 2492–2503, doi: 10.1190/1.1441880.
Panthulu, T. V., C. Krishnaiah, and J. M. Shirke, 2001, Detection of seepage paths in earth dams using self-potential and electrical resistivity methods: Engineering Geology, **59**, 281–295, doi: 10.1016/S0013-7952(00)00082-X.
Pelton, W. H., S. H. Ward, P. G. Hallof, W. R. Sill, and P. H. Nelson, 1978, Mineral discrimination and removal of inductive coupling with multifrequency IP: Geophysics, **43**, 588–609, doi: 10.1190/1.1440839.
Pengra, D., S. X. Li, and P. Wong, 1999, Determination of rock properties by low-frequency AC electrokinetics: Journal of Geophysical Research, **104**, 485–508, doi: 10.1029/1999JB900277.
Revil, A., 2012, Spectral induced polarization of shaly sands: Influence of the electrical double layer: Water Resources Research, **48**, W02517, doi: 10.1029/2011WR011260.
Revil, A., L. M. Cathles, S. Losh, and J. A. Nunn, 1998, Electrical conductivity in shaly sands with geophysical applications: Journal of Geophysical Research, **103**, 23925–23936, doi: 10.1029/98JB02125.
Revil, A., and N. Florsch, 2010, Determination of permeability from spectral induced polarization in granular media: Geophysical Journal International, **181**, 1480–1498, doi: 10.1111/j.1365-246X.2010.04573.x.
Revil, A., K. Koch, and K. Holliger, 2012, Relating grain size distribution to permeability and spectral induced polarization relaxation times in sands: Water Resources Research, **48**, W05602, doi: 10.1029/2011WR011561.
Revil, A., P. Leroy, and K. Titov, 2005, Characterization of transport properties of argillaceous sediments. Application to the Callovo-Oxfordian argillite: Journal of Geophysical Research, **110**, B06202, doi: 10.1029/2004JB003442.
Revil, A., N. Linde, A. Cerepi, D. Jougnot, S. Matthai, and S. Finsterle, 2007, Electrokinetic coupling in unsaturated porous media: Journal of Colloid and Interface Science, **313**, 315–327, doi: 10.1016/j.jcis.2007.03.037.
Revil, A., and M. Skold, 2011, Salinity dependence of spectral induced polarization in sands and sandstones: Geophysical Journal International, **187**, 813–824, doi: 10.1111/j.1365-246X.2011.05181.x.
Revil, A., W. F. Woodruff, and N. Lu, 2011, Constitutive equations for coupled flows in clay materials: Water Resources Research, **47**, W05548, doi: 10.1029/2010WR010002.
Salomon, D. K., G. K. Moore, L. E. Toran, and W. M. McMaster, 1992, A hydrologic framework for the Oak Ridge Reservation: ORNL/TM-12026. Oak Ridge, Tennessee: Department of Energy.
Saunders, J. A., and L. E. Toran, 1994, Evidence for dedolomitization and mixing in Paleozoic carbonates near Oak Ridge, Tennessee: Ground Water, **32**, 207–214, doi: 10.1111/j.1745-6584.1994.tb00635.x.
Schreiber, M. E., 1995, Spatial variability in groundwater chemistry in fractured rock: Nolichucky shale, Oak Ridge, TN: M.S. thesis, University of Wisconsin–Madison.
Schwarz, G., 1962, A theory of the low-frequency dielectric dispersion of colloidal particles in electrolyte solution: Journal of Physical Chemistry, **66**, 2636–2642, doi: 10.1021/j100818a067.
Seigel, H. O., 1959, Mathematical formulation and type curves for induced polarization: Geophysics, **24**, 547–565, doi: 10.1190/1.1438625.
Sheffer, M., 2007, Forward modeling and inversion of streaming potential for the interpretation of hydraulic conditions from self-potential data: Ph.D. thesis, The University of British Columbia.
Skold, M., and A. Revil, 2011, The pH dependence of spectral induced polarization of silica sands: Experiment and modeling: Geophysical Research Letters, **38**, L12304, doi: 10.1029/2011GL047748.
Slater, L., and D. Glaser, 2003, Controls on induced polarization in sandy unconsolidated sediments and application to aquifer characterization: Geophysics, **68**, 1547–1558, doi: 10.1190/1.1620628.
Slater, L., and D. P. Lesmes, 2002, Electrical-hydraulic relationships observed for unconsolidated sediments: Water Resources Research, **38**, 1213–1225, doi: 10.1029/2001WR001075.
Stern, O., 1924, Zur theorie der electrolytischen Doppelschicht (The theory of the electrolytic double layer): Zeitschrift für Elektrochemie, **30**, 508–516.
Vaudelet, P., A. Revil, M. Schmutz, M. Franceschi, and P. Bégassat, 2011a, Induced polarization signature of the presence of copper in saturated sands: Water Resources Research, **47**, W02526, doi: 10.1029/2010WR009310.
Vaudelet, P., A. Revil, M. Schmutz, M. Franceschi, and P. Bégassat, 2011b, Changes in induced polarization associated with the sorption of sodium, lead, and zinc on silica sands: Journal of Colloid and Interface Science, **360**, 739–752, doi: 10.1016/j.jcis.2011.04.077.
Vinegar, H. J., and M. H. Waxman, 1984, Induced polarization of shaly sands: Geophysics, **49**, 1267–1287, doi: 10.1190/1.1441755.
Watson, D. B., W. E. Doll, T. J. Gamey, J. R. Sheehan, and P. M. Jardine, 2005, Plume and lithologic profiling with surface resistivity and seismic tomography: Ground Water, **43**, 169–177, doi: 10.1111/j.1745-6584.2005.0017.x.
Watson, D. B., J. E. Kostka, M. W. Fields, and P. M. Jardine, 2004, The Oak Ridge Field Research Center Conceptual Model, NABIR FRC Technical Report: NABIR FRC. http://public.ornl.gov/orifc/FRC-conceptual-model.pdf.
Waxman, M. H., and L. J. M. Smits, 1968, Electrical conductivities in oil-bearing shaly sands: Journal of the Society of Petroleum Engineers, **8**, 107–122, doi: 10.2118/1863-A.
Weller, A., K. Breede, L. Slater, and S. Nordsiek, 2011, Effect of changing water salinity on complex conductivity spectra of sandstones: Geophysics, **76**, no. 5, F315–F327, doi: 10.1190/geo2011-0072.1.
Wilt, M. J., and D. K. Butler, 1990, Geotechnical applications of the self-potential (SP) method; Report 4: Numerical modelling of SP anomalies: documentation of program SPPC and applications: Technical Report REMR-GT-6. U. S. Army Corps of Engineers, Waterways Experiment Station.
Wilt, M. J., and R. F. Corwin, 1989, Numerical modeling of self-potential anomalies due to leaky dams: Model and field examples, *in* G. P. Merkler, H. Militzer, H. Hötzl, H. Armbruster, and J. Brauns, eds., Detection of subsurface flow phenomena: **27**, Springer-Verlag, 73–89.
Woodruff, W. F., and A. Revil, 2011, CEC-normalized clay-water sorption isotherm: Water Resources Research, **47**, W11502, doi: 10.1029/2011WR010919.
Zimmermann, E., A. Kemna, J. Berwix, W. Glaas, H. M. Münch, and J. A. Huisman, 2008, A high-accuracy impedance spectrometer for measuring sediments with low polarizability: Measurement Science and Technology, **19**, 105603, doi: 10.1088/0957-0233/19/10/105603.
Zundel, J. P., and B. Siffert, 1985, Mécanisme de rétention de l'octylbenzene sulfonate de sodium sur les minéraux argileux, *in* Solid-liquid interactions in porous media: Technip, 447–462.

Downloaded 01/22/13 to 138.67.207.132. Redistribution subject to SEG license or copyright; see Terms of Use at http://library.seg.org/